Nucleic Acids Research, 2025, **53**, gkaf107
https://doi.org/10.1093/nar/gkaf107
Gene regulation, Chromatin and Epigenetics

The NEXT complex regulates H3K27me3 levels to affect cancer progression by degrading G4/U-rich lncRNAs

Qianqian Yang[1,†], Zihan Zhou[1,†], Lian Li[1,†], Runhui Lu[1,†], Guofang Hou[1,†], Caihu Huang[1], Jiayi Huang[1], Hongyan Li[1], Yafan Zhang[1], Junya Li[1], Yixin Zhang[1], Anan Xu[1], Ran Chen[1], Yanli Wang[1], Xian Zhao[1], Jian Huang[1], Yiwei Wang[2,*], Xiaojing Zhao[1,*], Jianxiu Yu[1,*]

[1]Department of Biochemistry and Molecular Cell Biology & Department of Thoracic Surgery Ren Ji Hospital, Shanghai Jiao Tong University School of Medicine; Shanghai 200025, China
[2]Department of Urology, Ninth People's Hospital, Shanghai Jiao Tong University School of Medicine, Shanghai 200011, China

[*]To whom correspondence should be addressed. Email: Jianxiu.Yu@gmail.com
Correspondence may also be addressed to Xiaojing Zhao. Email: drzhaoxiaojing@aliyun.com
Correspondence may also be addressed to Yiwei Wang. Email: wang_yiwei@yeah.net
[†]The first five authors should be regarded as Joint First Authors.

Abstract

Polycomb repressive complex 2 (PRC2) is responsible for depositing H3K27me3 and plays essential roles in gene silencing during development and cancer. Meanwhile, the nuclear exosome targeting (NEXT) complex facilitates the degradation of numerous noncoding RNAs in the nucleoplasm. Here we find that the functional deficiency of the NEXT complex leads to an overall decrease in H3K27me3 levels. Specifically, ZCCHC8 depletion results in significant upregulation of nascent long noncoding RNAs (lncRNAs) containing G-quadruplex (G4) and U-Rich motifs (G4/U-Rich lncRNAs). The G4 motif binds to EZH2, blocking the chromatin recruitment of PRC2, while the U-Rich motif is specifically recognized by the NEXT complex for RNA exosome-mediated degradation. In tumor tissues with high ZCCHC8 expression in clear cell renal cell carcinoma (ccRCC) and lung adenocarcinoma (LUAD) patients, the NEXT complex excessively degrades nascent G4/U-Rich lncRNAs. Consequently, PRC2 core subunits are released and recruited to neighboring genomic loci, resulting in increased H3K27me3 levels and downregulation of adjacent genes, including tumor suppressors like *SEMA5A* and *ARID1A*. Notably, the EZH2 inhibitor Tazemetostat (EPZ-6438) exhibits greater sensitivity in cells with higher ZCCHC8 expression. Altogether, our findings demonstrate a novel mechanism that the NEXT complex regulates H3K27me3 levels by degrading nascent G4/U-Rich lncRNAs in cancer cells.

Graphical abstract

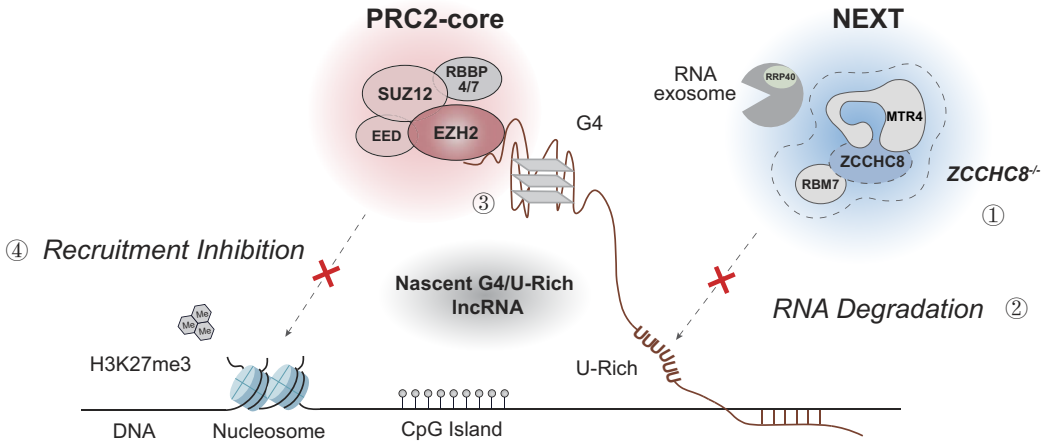

Introduction

The nuclear RNA exosome complex is the most ubiquitous RNA degradation machine in eukaryotes, which plays a central role in the 3′ to 5′ exo- and endo-processing of various RNAs and is crucial for RNA maturation, surveillance, turnover, and RNA quality control, further ensuring the integrity and function of the RNA pools [1, 2]. The nuclear RNA exosome functions optimally when it is associated with

Received: June 24, 2024. **Revised:** January 13, 2025. **Editorial Decision:** January 30, 2025. **Accepted:** February 5, 2025

cofactors that play crucial roles in recognizing and recruiting exosomes to a diverse array of RNA substrates [3]. These cofactors include the nuclear exosome targeting (NEXT) complex, the poly(A) exosome targeting (PAXT) complex, the polysome protector complex, as well as the TRF4-2-ZCCHC7-MTR4 polyadenylation (TRAMP) complex are the most thoroughly studied [4–7]. In the nucleoplasm, the NEXT complex is a key cofactor of the mammalian nuclear RNA exosome, which is a trimeric complex composed of the helicase hMTR4, the scaffold zinc-knuckle ZCCHC8 protein and the RNA recognition motif-containing RBM7 [8]. The NEXT complex is responsible for targeting promoter upstream transcripts (PROMPTs) [9], enhancer RNAs (eRNAs) [5], precursor telomerase RNAs [10], noncoding RNAs such as the 3′-extended products of snRNAs [11], and the newly synthesized RNAs [12].

Trimethylation of histone H3 lysine 27 (H3K27me3) is crucial for gene silencing and formation of facultative heterochromatin. This modification plays a vital role in cell fate determination, embryonic development, and tumorigenesis [13–15]. The Polycomb repressive complex 2 (PRC2), currently recognized as the sole multi-subunit complex in mammals responsible for H3K27me3, is indispensable for maintaining stem cell pluripotency and facilitating the development of multicellular organisms [16]. PRC2 is comprised of the core subunits Enhancer of Zeste 2 (EZH2) or its paralogue EZH1, SUZ12, EED, RBBP4, or RBBP7, as well as several auxiliary subunit [17]. EZH1/2 is the histone methyltransferase and serves as the catalytic subunit of PRC2. However, the complete catalytic activity of H3K27 methylation relies on the physical interaction between EZH2 and other core subunits of the complex. These interactions facilitate the deposition of H3K27me3 by regulating the complex stability and nucleosome-binding capacity [18]. Two different subcomplexes, PRC2.1 and PRC2.2, are formed by incorporating distinct combinations of auxiliary partners with the core subunit of PRC2 [19]. PRC2.1 consists of EPOP [20] or PALI [21] and one of the Polycomb-like (PCL) proteins (either PCL1/ PHF1, PCL2/ MTF2 or PCL3/ PHF19), while AEBP2 [22] and JARID2 [23] are found in PRC2.2. The auxiliary subunits promote the optimal catalytic activity of PRC2 through promoting the genomic targeting and/or enzymatic activities in different biological contexts [24].

PRC2 is extensively regulated by multiple factors, including DNA methylation and pre-existing histone modifications, such as H3K4me3, H3K36me2/3, and H2AK119ub1 [19]. It has been found that core subunits of PRC2, such as EZH2, SUZ12, and auxiliary subunits like JARID2 and AEBP2, exhibit RNA binding activity. Genome-wide analysis of the interactions between PRC2 and RNA through RNA immunoprecipitation sequencing (RIP-seq) reveals that PRC2 binds to RNA *in vivo* extensively [25–27]. Previous studies have proposed different models of RNA regulatory role in PRC2, including recruitment to target loci for epigenetic repression [28], eviction from chromatin [27, 29], and inhibition of catalytic activity [30]. Initially, it was believed that PRC2 engages in indiscriminate interactions with RNAs. However, recent evidence indicates that PRC2 selectively associates with specific RNA molecules. Notably, PRC2 shows a preference for RNA sequences containing short consecutive guanine repeats (G-tracts) and exhibits a stronger binding affinity for RNAs that fold into G-quadruplex (G4) structures, which removes PRC2 from chromatin [31]. Emerging reports indicate that PRC2 interacts with nascent RNAs through its EZH2 subunit, maintaining PRC2 activity in a poised state. Additionally, nascent RNAs compete with nucleosomes for binding to PRC2 [26, 32]. Furthermore, the PRC2 stability is compromised upon knockout (KO) of the ZFC3H1 component of the PAXT complex [33], another adaptor complex of RNA exosome in nucleoplasm. Transcriptional inhibition and nuclear RNA degradation in cells triggers PRC2 recruitment to CpG islands at active genes [27, 32], highlighting the close functional connection between RNA decay and PRC2 regulation. In our preliminary experiment, we identified a positive correlation between the levels of H3K27me3 and ZCCHC8, an essential subunit of the NEXT complex. This finding prompts the question: What is the relationship between the NEXT complex and the functional regulation of PRC2? However, to date, no research has established a functional connection between the NEXT complex and the PRC2 complex.

Mutations and deregulation in the PRC2-encoding genes frequently occur in a range of human cancers, accompanied by the abnormal global levels of H3K27me3 [15, 34, 35]. Elevated levels of EZH2 in breast cancer are associated with poor prognosis [36]. Therefore, pharmacological inhibition of EZH2 has become the focus of cancer epigenetic drug development and is under intensive investigation. Tazemetostat, EPZ-6438, is the first inhibitor drug targeting EZH2 approved by the FDA for the treatment of adult patients with locally advanced or metastatic epithelioid sarcoma [37]. Nevertheless, the combination therapy of EZH2 inhibitors and existing anticancer drugs is also a topic that requires further exploration.

Semaphorin-5A (Sema5A), a member of the class 5 subfamily of Semaphorins, functions as a bi-functional factor, exhibiting distinct roles in various types of cancer. Overexpression of Sema5A is linked to lymphangiogenesis, poor prognosis, and increased metastatic potential in cervical cancer cells [38], and it is similarly implicated in the progression of neuroendocrine pancreatic tumors [39]. In contrast, in lung adenocarcinomas (LUAD), SEMA5A functions as a tumor suppressor, as evidenced by both *in vitro* and *in vivo* experiments using nonsmall cell lung cancer cellular models. Additionally, the downregulation of SEMA5A in LUAD tissues is associated with poor overall survival [40]. Given the significant role of SEMA5A in cancer, the regulation of its expression merits further investigation.

In this study, we uncover a novel molecular mechanism by which the NEXT complex modulates H3K27me3 levels and impacts tumor progression. Specifically, loss of the key subunit ZCCHC8 or RBM7 within the NEXT complex results in a global reduction of H3K27me3 levels. Nascent G4/U-Rich long noncoding RNAs (lncRNAs) are accumulated due to the impaired NEXT complex in ACHN$^{ZCCHC8-/-}$ cells, which inhibits the binding of PRC2 to target gene loci and H3K27me3 deposition, thereby leading to increased expressions of adjacent genes and affecting cancer progression. Importantly, we provide evidence that combining EZH2 inhibitors with other anti-cancer drug may be a promising therapeutic strategy for patients of some cancers such as clear cell renal cell carcinoma (ccRCC) and LUAD with higher ZCCHC8 expression.

Materials and methods

Cell lines and clinical samples

Human embryonic kidney (HEK) 293T, 293FT, H1299, CAKI-1, A-498 were cultured in Dulbecco's modified Eagle's

medium (DMEM, Corning) supplemented with 10% fetal bovine serum (FBS, YEASEN), 1% penicillin/streptomycin (YEASEN) at 37°C in a humidified incubator with 5% CO_2. ACHN cells were grown in Eagle's minimum essential medium (MEM, Gibco) supplemented with 10% FBS, 1% penicillin/streptomycin, 1% MEM nonessential amino acids (NEAA, Gibco), and 1% sodium pyruvate (Gibco) at 37°C in a humidified incubator with 5% CO_2. HK-2 cells were cultured in DMEM/Nutrient Mixture F-12 (DMEM/F-12, Gibco) supplemented with 10% FBS, 1% penicillin/streptomycin at 37°C in a humidified incubator with 5% CO_2. ACHN cells and HK-2 cells were purchased from the Cell Bank/Stem Cell Bank, Chinese Academy of Sciences, Shanghai, China. CAKI-1 cells and A-498 cells are kind gifts from Renji Hospital, Shanghai, China. Murine embryonic stem cells CGR8 [41], cultured in ESC medium Glasgow's Minimum Essential Medium (GMEM, Gibco) supplemented with 15% FBS, 1 × sodium pyruvate, 1 × NEAA, 1000 U/ml (Sigma), 0.1 mM β-mercaptoethanol and 2 mM L-glutamine. ZCCHC8-KO ACHN cell line was generated by the CRISPR-Cas9 technology, and all stable knockdown cell lines as well as overexpressing cell lines were generated by the lentiviral system. For transient expressions, cells were transfected with the plasmid constructs using Lipofectamine 2000 (Invitrogen) and analyzed 48 h after transfection.

With informed consent signed by the patients and approved by the Medical Ethics Committee, clinical samples were strictly tested in accordance with ethical requirements. The renal clear cell carcinoma tumor specimens were obtained from the Shanghai Ninth People's Hospital, and the assigned approval number of the ethical approval is SH9H-2019-A444-1. The LUAD tumor specimens were obtained from Shanghai Renji Hospital, and the assigned approval number of the ethical approval is RA-2022-159.

Antibodies and reagents

The antibodies mentioned are all commercial antibodies, as follows: ZCCHC8 (Proteintech), RBM7 (Proteintech), MTR4 (Proteintech), EZH2 (Cell Signaling Technology), SUZ12 (Cell Signaling Technology), EED (Abclonal), RRP40 (Abclonal), RBBP4 (Abclonal), SEMA5A (Bioss), Histone H3 (Abcam), H3K27me3 (Cell Signaling Technology), H3K27ac (Abcam), H2AK119ub1 (Cell Signaling Technology).

To inhibit the transcription of nascent RNA, cells with 70%–80% confluency were treated with 5,6-dichlorobenzimidazole 1-β-D-ribofuranoside (DRB, Sigma) in culture medium at a concentration of 60 or 100 μM for 3 h. The cells were washed twice with phosphate-buffered saline (PBS) to remove the DRB, and then the cells were subjected to chromatin isolation experiment. Pazopanib (Selleckchem) and/or the EZH2 inhibitor EPZ-6438 (Selleckchem) were added to the cells at the concentration indicated in the figures for 48 h. Following the treatment, the cells were prepared for immunoblotting or cell viability analysis, as detailed below. All reagents used in this study are listed in Supplementary Table S1.

Plasmids, short hairpin RNAs and small guide RNAs

Human ZCCHC8 was amplified by polymerase chain reaction (PCR) using KOD-plus Kit (TOYOBO) and was inserted using the *BamH*I and *Xho*I sites of the pCMV-tag2B vector, obtaining the expression plasmid Flag-ZCCHC8-WT. The Flag-ZCCHC8-ΔZnK was constructed by deleting the amino acid region from 228 to 244 in the plasmid Flag-ZCCHC8-WT. The ZCCHC8-L295/299E mutant (not interacting with RBM7) was generated using the KOD-plus-mutagenesis Kit (TOYOBO) according to the manufacturer's protocol. For stable expression, the Flag-ZCCHC8 was inserted using the *BamH*I and *Xho*I sites of the lentiviral vector CD513B. The lncRNAs ARID1A-AS and SNHG18 were subcloned into the CD513B vector using the *EcoR*I and *Not*I sites, and the G4-mutants were obtained by mutating 'G' to 'A' in the predicted G4 sequences of ARID1A-AS and SNHG18. To purify prokaryotically expressed proteins, EZH2 and RBM7 were subcloned into the pGEX-4T-1 vector. The short hairpin RNA (shRNA) oligonucleotides for ZCCHC8, RBM7 and RRP40 referred from Sigma inserted using the *Age* I and *EcoR*I sites of the lentiviral vector pLKO.1. The sequences of all plasmids were verified by sequencing. All sequences for plasmid construction primers, shRNAs and small guide RNAs(sgRNAs) are listed in Supplementary Table S2.

Western blotting analysis

To prepare protein extracts for immunoblot analysis, stable cell lines were washed twice with cold PBS, scraped from the dishes in sodium dodecyl sulphate (SDS) lysis buffer (50 mM Tris–HCl, 150 mM NaCl, 2% SDS). The same buffer was used to prepare protein extracts from clinical samples and chromatin pellet obtained during chromatin isolation assay. Samples were heated at 95°C for 10 min and sonicated. The lysates were centrifuged at maximum speed (17 000 × *g*) for 30 min at 4°C. The supernatant was collected in a fresh tube and the protein concentration was measured using Nanodrop 2000 (Thermo Fisher Scientific). The protein extracts were separated by SDS–polyacrylamide gel electrophoresis before transferring onto polyvinylidene fluoride membrane, followed by incubation with primary antibodies and horseradish peroxidase-linked secondary antibodies.

RNA extraction and Quantitative reverse transcription-Polymerase Chain Reaction

For lncRNA and messenger RNA (mRNA) expression profiling, total RNA was extracted by TRIZOL reagent (Sigma–Aldrich) and then treated with DNase I (Thermo Fisher Scientific) to degrade genomic DNA. Reverse transcription was performed by using the PrimeScript RT-PCR Kit (TAKARA) following the manufacturer's instructions. Quantitative real-time polymerase chain reaction (qRT-PCR) was performed with qPCR SYBR Green Master Mix (Vazyme) to analyze the indicated RNA abundance. Primers used for qRT-PCR are listed in Supplementary Table S2.

Co-immunoprecipitation

Cells transfected with indicated plasmids or stable cell lines were lysed with radio-immunoprecipitation assayRIPA) lysis buffer [50 mM Tris–HCl, pH7.4, 150 mM NaCl, 1% NP-40, 0.1% SDS, 1 mM ethylenediaminetetraacetic acid (EDTA), pH 8.0, protease inhibitor cocktail] on ice for 30 min. Cell lysates were sonicated and centrifuged at maximum speed (17 000 × *g*) for 30 min at 4°C. The supernatant was incubated with protein A/G-agarose beads and indicated antibodies at 4°C overnight, and then washed for five times with RIPA lysis

buffer without protease inhibitor cocktail and subjected to western blotting (WB) analysis.

Chromatin isolation with RNase A treatment

RNase A treatment and cell fractionation were performed as previously described [27]. ACHN$^{ZCCHC8\text{-}WT}$ and ACHN$^{ZCCHC8\text{-}/-}$ cells were trypsinized, washed twice with PBS, permeabilized with 0.05% Tween-20 in PBS for 10 min on ice, washed once, resuspended with PBS, and mock-treated or treated with 0.2 mg/ml RNase A for 30 min at room temperature (RT). Cells were centrifuged at 1200 rpm, washed twice with PBS before proceeding with chromatin isolation. The pellet was resuspended in buffer A (10 mM, HEPES, pH 7.9, 10 mM KCl, 1.5 mM $MgCl_2$, 10% glycerol, 0.34 M sucrose, 1 mM dithiothreitol (DTT), 0.1 mM phenylmethylsulfonyl fluoride (PMSF), 0.1% Triton X-100, and protease inhibitor cocktail), and incubated for 5∼10 min on ice. Nuclei were collected by low-speed centrifugation (1300 × *g*) for 5 min at 4°C. The supernatant (cytoplasmic fraction) was further clarified by high-speed centrifugation (17 000 × *g*) for 15 min at 4°C to remove cell debris and insoluble aggregates. Nuclei were washed once in buffer A, and then lysed in buffer B (3 mM EDTA, 0.2 mM EGTA, 1 mM DTT, protease inhibitor cocktail). Insoluble chromatin pellet was collected by centrifugation (1700 × *g*) for 4 min at 4°C, washed once with buffer B and centrifuged again under the same conditions. The final chromatin pellet (chromatin fraction) resuspended in SDS buffer followed by western blotting analysis.

RNA immunoprecipitation

The RNA immunoprecipitation (RIP) assay was performed as previously described [42, 43]. Briefly, cells transfected with indicated plasmids or stable cell lines were lysed with RIP lysis buffer [50 mM Tris–HCl, pH7.4, 150 mM NaCl, 1% NP-40, 2 mM $MgCl_2$, 400 μM Ribonucleotide Vanadyl Complex (RVC, New England BioLabs), 40 U/μl RiboLock RNase Inhibitor, protease inhibitor cocktail] on ice for 30 min. Cell lysates were sonicated and centrifuged at maximum speed (17 000 × *g*) for 30 min at 4°C. One-tenth of the lysates were used as input-RNA, while 1/50 of lysates were saved as input-protein for western blotting to detect the protein expression, and left lysates were incubated with protein A/G-agarose beads and indicated antibodies at 4°C overnight. Beads bound with RNAs were washed for 3–5 times with RIP lysis buffer. One-tenth of the beads were subjected to western blotting analysis to identify the efficiency of immunoprecipitation, and the others were treated with TRIZOL reagent (Sigma–Aldrich) to extract the RNAs bound to specific antibody (RIP-RNA). RIP-RNA and input-RNA were subjected to qRT-PCR and analyzed using the $2^{-\Delta\Delta CT}$ method.

Chromatin immunoprecipitation-qPCR

For chromatin immunoprecipitation (ChIP), cells were fixed in 1% formaldehyde (Sigma) for 10 min and then quenched with 125 mM glycine. Subsequently, the cells were resuspended in ChIP lysis buffer (50 mM Tris–HCl, pH 7.5, 150 mM NaCl, 5 mM EDTA, 0.5% NP-40, 1% Triton X-100, 0.5% SDS). The chromatin was sonicated to achieve fragments with a size of 200–500 bp. After centrifugation at maximum speed (17 000 × *g*) for 10 min at 4°C, the supernatant was incubated with protein A/G-agarose beads and indicated antibodies at 4°C overnight, and then washed for five times with ice-cold ChIP wash buffer (50 mM HEPES-KOH, pH 7.5, 500 mM LiCl, 1 mM EDTA, 1% NP-40, 0.7% sodium deoxycholate), once with Tris-EDTA (TE) buffer (10 mM Tris–HCl, pH 8.0, 1 mM EDTA, 50 mM NaCl). The immune-complexes were eluted with ChIP elution buffer (50 mM Tris–HCl, pH 8.0, 10 mM EDTA, 1% SDS) and de-crosslinked overnight at 65°C with 0.2 M NaCl. Following treatment with RNase A (Cell Signal Technology) and Proteinase K (Millipore), the DNA fragments were purified using Cycle-Pure Kit (Omega). The relative immunoprecipitated DNA was determined by quantitative PCR using the $2^{-\Delta\Delta CT}$ method, with IgG samples as the enrichment controls.

Purification of GST-proteins

This method has been previously described [42, 43]. Briefly, the prokaryotic expression constructs pEGX-4T1-EZH2 and pEGX-4T1-RBM7 were transformed into competent cell BL21 and were induced with 0.5 mM isopropyl β-d-1-thiogalactopyranoside for 12–16 h at 16°C. The bacterial pellet was resuspended in buffer (50 mM Tris–HCl, pH 7.4, 150 mM NaCl, pH 7.4) and sonicated. After centrifuging at maximum speed (17 000 × *g*) for 20 min at 4°C, the bacterial solution passed through a filter column containing GST-Sefinose Resin (Sangon) to capture the GST-protein, and then eluted with glutathione (GSH) buffer (50 mM Tris–HCl, pH 8.0, 20 mM GSH). The purified protein was detected by coomassie brilliant blue staining and western blotting.

Electrophoretic mobility shift assay

Predicted G4 RNA sequences and U-Rich RNA sequences of ARID1A-AS and SNHG18 were synthesized by Gene-Pharma Co., Ltd. and labeled with biotin at 5′-end. The RNA was heated at 95°C for 3 min, and then renatured with binding buffer (50 mM Tris–HCl, pH 7.5, 100 mM KCl, 2.5 mM $MgCl_2$, 2 mM 2-mercaptoethanol, 0.1 mg/ml bovine serum albumin, 5% glycerol, 0.05% NP-40, protease inhibitor cocktail) at 37°C for 30 min. Purified GST-EZH2 or GST-RBM7 was incubated with the renatured RNA in binding buffer at RT for 30 min, The reactions were separated on native 7% polyacrylamide gels. Sequences of synthesized RNAs are listed in Supplementary Table S2.

Wound healing assay

For the wound healing assay, the sterile culture-inserts (IBIDI) were placed in 12-well plates, and the stable cell lines were seeded in the culture-inserts for 24 h to get confluent monolayer. Remove the culture-inserts and cells were continued to culture in serum-free DMEM for migration. Photos were taken as indicated time until the wound was healed.

Soft agar colony formation assay

The effect of ZCCHC8 on anchorage-independent growth was determined by a soft agar colony forming assay as described previously [44, 45]. Briefly, stable cells were suspended in 2 mL of colony formation gel (2 × medium, 10% FBS, 1% penicillin/streptomycin, and 3.5% agar gel), and added to 6-well plates coated with 2 mL of base gel (2 × medium, 10% FBS, 1% penicillin/streptomycin and 0.6% agar gel). Then, cells were cultured at 37°C in a humidified atmosphere containing 5% CO_2 for 3–4 weeks. Gels with viable colonies

were stained with 0.005% crystal violet and the numbers of colonies were counted.

Xenograft tumor model

The nude mice involved in the study were purchased from Shanghai Lingchang Biotechnology Co., Ltd. and housed in specific pathogen-free environments. The experiment of the xenograft tumor model was established as described previously [46]. Stable ACHN cell lines were injected subcutaneously into 6-week-old nude mice ($n = 8$) at the final concentration of 2.5×10^6 cells. Mice were sacrificed 3 weeks later, and tumors were weighed and photographed. All animal experiments were conducted in accordance with the Guidelines for the Care and Use of Laboratory Animals and approved by the Institutional Animal Care and Use Committee of Shanghai Jiao Tong University School of Medicine.

Cell viability and proliferation

For cell viability assay, cells were seeded at a density of 5000 cells per well in 96-well plates, and treated with pazopanib and/or EPZ-6438 at the indicated concentration for 48 h. After treatment, the cellular activity was measured by Cell Counting Kit-8 kit (YEASEN) following the manufacturer's instruction. The relative viability of cells was analyzed by the ratio of absorbance under drug treatment to dimethyl sulfoxide (DMSO) treatment. For cell proliferation assay, cells were seeded at a density of 1500 cells per well in 96-well plates. The capability of cell proliferation was measured at indicated time points using Cell Counting Kit-8 kit (YEASEN) according to the manufacturer's protocol.

Drug cytotoxicity and plate colony formation assay

Cells were seeded at a density of 1500 cells/well on 12-well plates, and treated with indicated drugs. Medium was replaced with fresh drug-containing medium every 3 days. After 7–14 days, colonies were stained with 0.1% crystal violet overnight, and the area of colonies was measured by Image J.

RNA-seq analysis

For RNA-seq, total RNA extracted from indicated stable ACHN cell lines by TRIZOL reagent was used for removing the ribosomal RNAs (rRNAs) with NEBNext rRNA Depletion Kit (New England Biolabs) as the manufacturer's instructions. A total of 150 base paired-end reads were harvested from illumina Novaseq 6000 sequencer, and were quality controlled by Q30. After 3′ adaptor-trimming and low quality reads removing by cutadapt software (v1.9.3). The high quality reads were aligned to the human reference genome (UCSC hg19) with hisat2 software (v2.0.4) [47]. Then, cuffdiff software (v2.2.1, part of cufflinks) [48] was used to get the Fragments Per Kilobase of exon model per Million mapped fragments (FPKM) as the expression profiles of lncRNA and mRNA, and fold change and *P*-value were calculated based on FPKM, differentially expressed lncRNA and mRNA were identified. LncRNA target genes were predicted by the locations to nearby genes. Pathway enrichment was performed using Gene Set Enrichment Analysis version 4.2.2 [49].

ChIP-seq analysis

For ChIP-seq, ChIP was performed with GenSeq® ChIP Kit (GenSeq Inc.) according to the manufacturer's instructions for the ACHN$^{ZCCHC8\text{-}WT}$ cells and ACHN$^{ZCCHC8\text{-}/-}$ cells with a single biological replicate. The yield of ChIPed DNA was determined via Quant IT fluorescence assay (Thermo Fisher), and sequencing libraries were generated with GenSeq® Rapid DNA Library Prep Kit (GenSeq Inc.) by following the manufacturer's manual. The library quality was determined by using Agilent 2100 Bioanalyzer (Agilent), and then, subjected to high-throughput 150 base paired-end sequencing on Illumina NovaSeq sequencer. Raw data were generated after sequencing, image analysis, base calling and quality filtering on Illumina Novaseq6000 sequencer. First, Q30 was used to perform quality control. After adaptor-trimming and low quality reads removing by cutadapt (v1.9.3) software, high quality clean reads were generated. Then these clean reads were aligned to reference genome using bowtie2 software (v2.2.4) with default parameters [50]. Peak calling was performed with MACS software (v2.2.7.1) [51]. Differentially enriched peaks (DEPs) were identified by diffReps software (v1.55.4) [52], with the *P*-value < 0.0001 and fold change ≥ 2 as the difference threshold, and the G-test was used to identify the differentially enriched peaks. The enriched peaks were then annotated with the latest UCSC RefSeq database to connect the peak information with the gene annotation. ChIP-seq signal within 2.5 kb upstream and downstream of the peak was analyzed using DeepTools software [53]. Genome alignment files of RNA-seq and ChIP-seq were visualized using EPGG genome browser (http://epigenomegateway.wustl.edu/browser/) [54].

RNA-seq and ChIP-seq high throughput sequencing were all performed by Cloud-Seq Biotech (Shanghai, China). All the raw data have been deposited in the Gene Expression Omnibus under accession code GSE243767.

SLAM-seq analysis

Thiol (SH)-linked alkylation for metabolic RNA sequencing (SLAM-seq) was performed as described [55]. Briefly, ACHN$^{ZCCHC8\text{-}WT}$ cells and ACHN$^{ZCCHC8\text{-}/-}$ cells were grown to the proper cell density. The final concentration of 4-thiouridine (s^4U) was ensured to reach 100 μM. After 1 h of incubation, the culture medium was immediately removed. Cells were washed twice in PBS. Total RNA was extracted with Trizol (Invitrogen), and then treated with iodoacetamide under optimal reaction conditions. rRNA was removed from the samples by the GenSeq® rRNA Removal Kit (GenSeq, Inc.) kit. The rRNA-depleted samples were subjected to library construction with GenSeq® Low Input RNA Library Prep Kit (GenSeq, Inc.) according to the manufacturer's instructions. Paired-end reads were harvested from Illumina NovaSeq sequencer, and were quality controlled by by Q30, FastQC, and FastQ Screen. 3′ adaptor- and low quality reads were trimmed by cutadapt software (v1.9.3), the high quality trimmed reads (clean reads) were aligned to the reference genome using NextGenMap with default parameters. The mismatch of T to C sites were extracted by VarScan2 software [56]. Any called T to C SNPs from this dunk will be excluded in the subsequent analyses to reduce the false-positive number.

Motif analysis of nascent lncRNAs was performed online using the MEME Suite website (https://meme-suite.org/meme/tools/meme) [57]. The R package G4iMGrinder [58] and the online prediction tool QGRS Mapper (https://bioinformatics.ramapo.edu/QGRS/index.php) [59] were used to G4 pre-

diction of the 2-fold upregulated nascent lncRNAs (fold change ≥ 2) in ACHN$^{ZCCHC8-/-}$ cells.

High throughput sequencing of SLAM-seq was performed by Cloud-Seq Biotech (Shanghai, China). All the raw data have been deposited in the Gene Expression Omnibus under accession code GSE284433.

Statistical analysis

Statistical analyses were performed with GraphPad Prism 8. Data are presented as the means ± standard deviation (SD) for qPCR, soft-agar colony formation assay, xenograft tumor model and clinical data analysis. The simple linear regression correlation analysis was performed to analyze the association between the expressions of ZCCHC8 with SEMA5A and ARID1A expression levels. One-way Analysis of Variance (ANOVA) or unpaired two-tailed Student's *t*-tests were applied for statistical analysis. $P < .05$ (*), $P < .01$ (**), and $P < .001$ (***) were considered statistically significant.

Results

The NEXT complex positively regulates H3K27me3 levels

To investigate the functional connection between NEXT and PRC2 complexes, it is first necessary to determine whether the NEXT complex affects the level of H3K27me3. We observed that the expression levels of ZCCHC8, a key component of the NEXT complex, were higher in an advanced ccRCC cell line ACHN and lower in normal cell line HK2 (an immortalized proximal tubule epithelial cell line from normal adult human kidney) and ccRCC cell line CAKI-1 (Supplementary Fig. S1A and B). Compared to HK-2 and CAKI-1, ACHN cells also exhibited higher levels of H3K27me3 (Supplementary Fig. S1C), indicating a positive correlation between ZCCHC8 and H3K27me3 levels. Therefore, we used the CRISPR/Cas9 technology to knock out ZCCHC8, disrupting the assembly and function of the NEXT complex in ACHN cells (Fig. 1A). Genomic DNA sequencing showed that the base 'C' at the position 148 in the first exon of *ZCCHC8* was deleted in ACHN$^{ZCCHC8-/-}$ cells (Fig. 1B), which resulted in a complete loss of ZCCHC8 protein expression (Supplementary Fig. S1D). We found that the deletion of ZCCHC8 in ACHN cells led to a marked decrease in H3K27me3 level (Fig. 1C). In order to validate this result, we designed two shRNAs targeting ZCCHC8, designated as shZCCHC8-1 and shZCCHC8-2. We then constructed stable ZCCHC8-knockdown cell lines in ACHN and HEK 293T cells using a lentiviral infection system (Supplementary Fig. S1E and F). Western blotting analyses indicated that the knockdown of ZCCHC8 resulted in reduced levels of H3K27me3 in both ACHN and 293T cells. Since the knockdown efficacy of shZCCHC8-1 was lower than that of shZCCHC8-2, we proceeded with the latter for the generation of additional stable knockdown cell lines, including CAKI-1, A-498, and LUAD cell line H1299, which exhibited significantly decreased H3K27me3 levels (Fig. 1C and G). To further verify our findings, we utilized two additional shRNAs targeting murine ZCCHC8 (murine shRNA-1 and murine shRNA-2) to establish ZCCHC8 knockdown stable cell lines in murine embryonic stem cells (CGR8) via the lentiviral infection system. Western blotting results demonstrated that the knockdown of ZCCHC8 significantly reduced H3K27me3 levels in CGR8 cells (Fig. 1D), consistent with the observations in human tumor cell lines. Conversely, stable overexpression of Flag-ZCCHC8 in CAKI-1 resulted in a significant upregulation of H3K27me3 levels (Fig. 1E). Consistently, the decreased H3K27me3 levels were rescued and increased after restoring expression of Flag-ZCCHC8 in either ACHN$^{ZCCHC8-/-}$ (Fig. 1F) or H1299-shZCCHC8 (Fig. 1G). In contrast, other histone modifications including H3K27ac, H3K4me3 and H2AK119ub1 were almost unaffected by changes in ZCCHC8 levels (Supplementary Fig. S1G–I), implying that the NEXT complex specifically regulates the H3K27me3 level. Therefore, the above results indicate that ZCCHC8, as a key component of the NEXT complex, has a positive regulatory effect on H3K27me3 levels in different cells.

We further performed the ChIP-seq to validate the impact of ZCCHC8 deficiency on H3K27me3 deposition in genome-wide. Compared with ACHN$^{ZCCHC8-WT}$ cells, KO of ZCCHC8 in ACHN$^{ZCCHC8-/-}$ cells resulted in a significant decrease in H3K27me3 signaling in the 2.5-kb upstream and downstream regions of the peak center (Fig. 1H and I). Together, these findings demonstrate that the impaired NEXT complex leads to a significant decrease in H3K27me3 levels and promotes chromatin accessibility (Fig. 1J).

ZCCHC8 promotes chromatin recruitment of PRC2 core subunits through RNA

PRC2 is the only complex found to have H3K27me3 catalytic activity, consisting of four core subunits EZH1/2 (mainly EZH2), EED, SUZ12 and RBBP4/RBBP7 (Supplementary Fig. S2A) and multiple auxiliary subunits [17]. To investigate the mechanism by which the NEXT complex regulates H3K27me3, we first assessed whether ZCCHC8 deficiency affects the protein levels of key subunits or the integrity of PRC2 complex. Western blotting results confirmed that the expression levels of PRC2 core subunits EZH2, SUZ12, EED, and RBBP4 were not affected by either ZCCHC8 knocking out (ACHN$^{ZCCHC8-/-}$ cells) or ZCCHC8 knocking down (H1299-shZCCHC8 cells) (Fig. 2A and Supplementary Fig. S2B). The catalytic activity of EZH2 is dependent on other core subunits of PRC2, including SUZ12 and EED, which are crucial for the integrity of PRC2. Additionally, RBBP4/7 can stabilize the binding of the PRC2 core subunits with histones. Considering this, we wondered whether ZCCHC8 affects the interaction between the core subunits of PRC2. Co-immunoprecipitation (Co-IP)/western blotting results revealed that the interactions between EZH2 and other core subunits, SUZ12, EED, and RBBP4, were not affected by the deletion of ZCCHC8 in ACHN$^{ZCCHC8-/-}$ cells (Fig. 2B). Similarly, the same results were obtained in 293T cells knocking down ZCCHC8 (Supplementary Fig. S2C). Moreover, lysates from ACHN$^{ZCCHC8-/-}$ cells and CAKI-1 cells knocking down ZCCHC8 were Co-IP with anti-SUZ12 antibody, respectively. The results showed that the interactions between SUZ12 and EZH2, EED, or RBBP4 were also not affected by ZCCHC8 deletion or knockdown (Fig. 2C and Supplementary Fig. S2D).

Next, we aimed to investigate whether ZCCHC8 regulates the recruitment of PRC2 to chromatin. Given that EZH2 is the core catalytic subunit of PRC2, we performed ChIP-seq analysis on EZH2 to determine whether the deficiency of ZCCHC8 results in reduced chromatin recruitment of EZH2. The ChIP-seq results demonstrated that EZH2 signals were significantly weakened in ACHN$^{ZCCHC8-/-}$ cells (Fig. 2D).

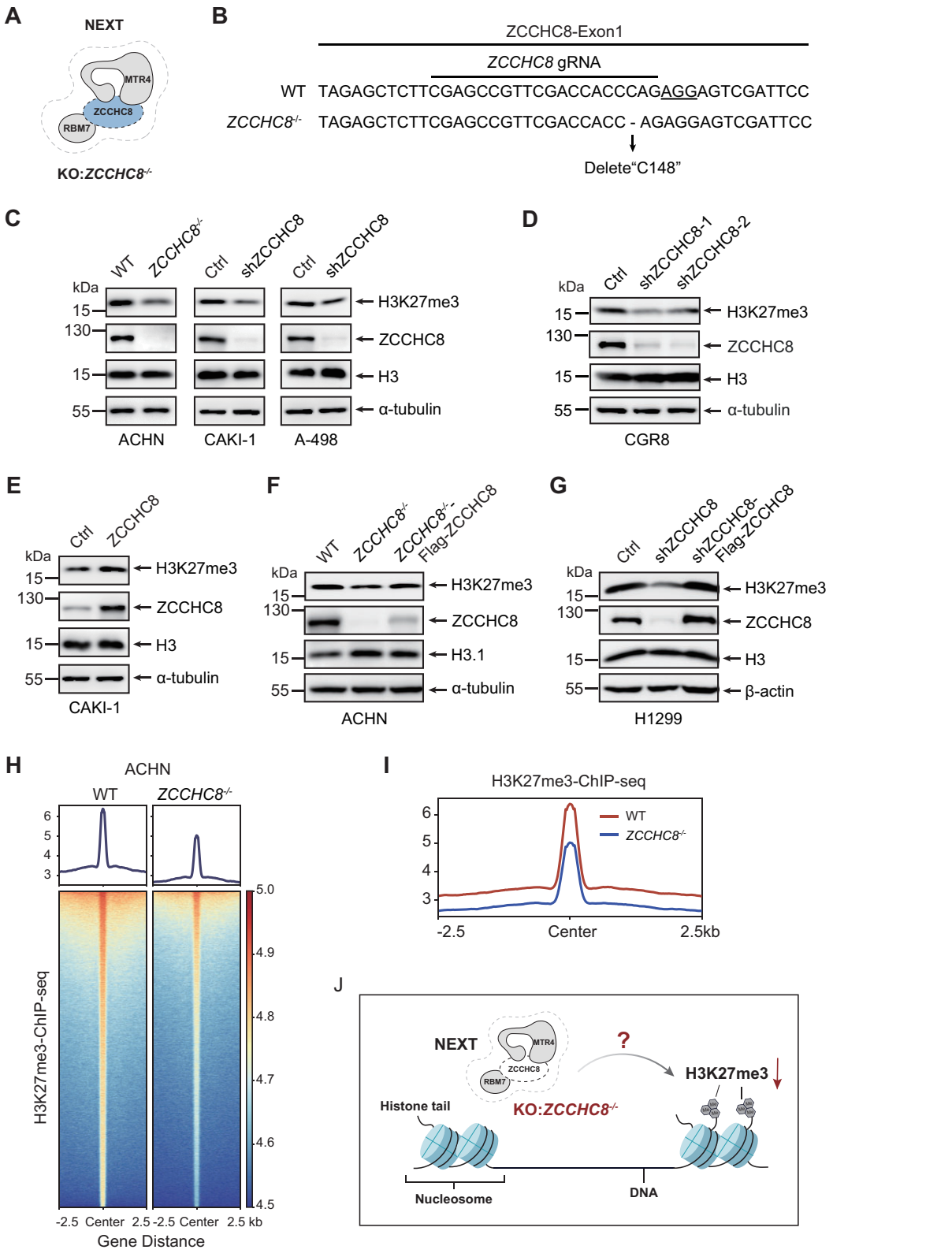

Figure 1. H3K27me3 levels are decreased in ZCCHC8-deficient cells. (**A**) Schematic diagram of the NEXT complex. (**B**) *ZCCHC8*-KO ACHN cell line (ACHN$^{ZCCHC8-/-}$) was constructed by the CRISPR-Cas9 system, and genomic DNA sequencing confirmed the deletion of base 'C' at position 148 in the first exon of ZCCHC8. (**C, D**) KO or knockdown of ZCCHC8 led to a decrease of H3K27me3 levels. ZCCHC8-knockdown cell lines were constructed by the lentiviral system using shRNA-2 targeting human ZCCHC8 in CAKI-1 and A-498 cells. For CGR8 cells, murine shRNA-1 and shRNA-2 were used to construct stable ZCCHC8-knocking down cells. The levels of ZCCHC8 and H3K27me3 in the above cells and ACHN$^{ZCCHC8-/-}$ cells were detected by western blotting; H3 and α-tubulin were used as loading controls. (**E–G**) The levels of ZCCHC8 and H3K27me3 in CAKI-1 cells stably overexpressing Flag-ZCCHC8 (**E**), ACHN$^{ZCCHC8-/-}$ cells stably re-expressing Flag-ZCCHC8 (**F**), and H1299-shZCCHC8 cells (using shZCCHC8-2) stably re-expressing Flag-ZCCHC8 were detected by western blotting (**G**). Heatmap (**H**) and H3K27me3 ChIP-seq read densities (**I**) at the H3K27me3 peaks called in ACHN$^{ZCCHC8\text{-}WT}$ cells and ACHN$^{ZCCHC8-/-}$ cells. Each row of the heatmap illustrates the ChIP-seq read density across regions extending ± 2.5 kb from the center of the peak. (**J**) Schematic diagram of NEXT complex negatively regulating H3K27me3.

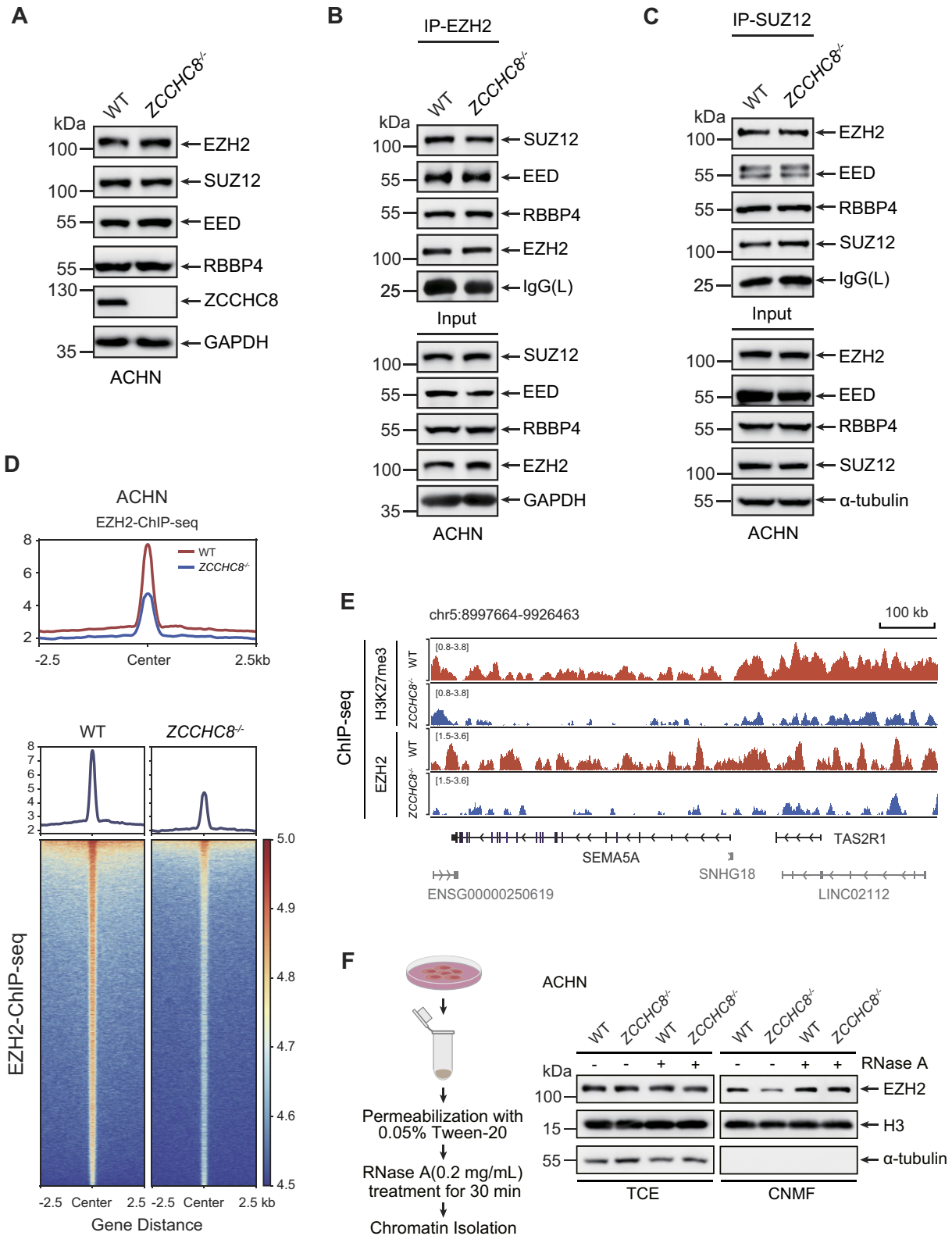

Figure 2. ZCCHC8 promotes the chromatin occupancy of PRC2 core subunits in an RNA-dependent manner. (**A**) Western blotting analysis of PRC2 core subunits expression in ACHN$^{ZCCHC8-/-}$ cells. (**B**) Co-IP/western blotting (Co-IP/WB) analysis of the interactions between EZH2 and other key subunits of PRC2 complex, including SUZ12, EED, and RBBP4 in ACHN$^{ZCCHC8-/-}$ cells. (**C**) Co-IP/WB to detect the interactions between SUZ12 and other core subunits of PRC2 complex, including EZH2, EED, and RBBP4 in ACHN$^{ZCCHC8-/-}$ cells. (**D**) The EZH2 ChIP-seq read densities (upper) and heatmap (lower) at the EZH2 peaks called in ACHN$^{ZCCHC8-WT}$ cells and ACHN$^{ZCCHC8-/-}$ cells. Each row of the heatmap illustrates the ChIP-seq read density across regions extending ± 2.5 kb from the center of the peak. (**E**) Representative genome browser tracks for H3K27me3, EZH2 signal peaks in ACHN$^{ZCCHC8-WT}$ and ACHN$^{ZCCHC8-/-}$ cells. (**F**) Experimental flowchart for cell permeabilization and RNase A treatment (left). In ACHN cells, ZCCHC8 deletion resulted in a reduction of EZH2 levels in chromatin fractions without RNase A treatment, while it had no effect in the presence of RNase A. TCE refers to the total cell extract (left), and CNMF refers to the chromatin nuclear matrix bound fraction (right).

Peaks of both EZH2 and H3K27me3 on a representative genomic segment including *SEMA5A*, *TAS2R1*, *SNHG18*, *LINC02112*, *ENSG00000250619* genes in ACHN$^{ZCCHC8\text{-}/-}$ cells were clearly lower than those in ACHN$^{ZCCHC8\text{-}WT}$ cells (Fig. 2E).

Considering the crucial role of nuclear RNA in regulating PRC2 function, as well as the involvement of the NEXT complex in targeting and delivering various nuclear RNAs to nuclear RNA exosomes for degradation, we first hypothesized that the effect of ZCCHC8 on EZH2 recruitment to chromatin may be mediated by nuclear RNA. To test this hypothesis, we assessed the impact of RNA presence or absence on ZCCHC8-mediated regulation of EZH2 recruitment by adding RNase A or omitting it, respectively. ACHN$^{ZCCHC8\text{-}WT}$ and ACHN$^{ZCCHC8\text{-}/-}$ cells were subjected to RNase A treatment after permeabilized with 0.05% Tween-20, followed by chromatin separation and western blotting analysis [27] (Fig. 2F). The results showed that in the absence of RNase A, the level of EZH2 in the chromatin fraction significantly decreased following the KO of ZCCHC8 (Fig. 2F, lanes 5 and 6). In contrast, when RNase A was added, the level of EZH2 in the chromatin fraction remained unaffected by the absence of ZCCHC8 (Fig. 2F, lanes 7 and 8). The results demonstrated that the inhibitory effect of ZCCHC8 on the chromatin recruitment of EZH2 was abolished upon the addition of RNase A. Collectively, these results suggest that ZCCHC8 facilitates the binding of PRC2 core subunit EZH2 to the chromatin in an RNA-dependent manner, thereby increasing the H3K27me3 deposition on the chromatin.

ZCCHC8 deficiency upregulates the levels of nascent G4/U-rich lncRNAs

Dysfunctions in the NEXT complex result in metabolic disturbances of RNAs, including promoter upstream transcripts (PROMPTs) [9], eRNAs [5], precursor telomerase RNAs [10], 3′-extended products of snRNAs [11], and nuclear nascent RNAs [12]. Having discovered the RNA-dependent regulation of EZH2 chromatin recruitment by ZCCHC8 (Fig. 2F), we further investigated which type of substrate RNA is responsible for this regulation. RNA sequencing (RNA-seq) revealed that KO of ZCCHC8 led to a significant increase in the expression levels of numerous lncRNAs (Supplementary Fig. S3A). Further analysis of the loci of upregulated lncRNAs revealed that over 67.9% of these lncRNAs are located within 1 kb of their neighboring gene promoters (Supplementary Fig. S3B), suggesting that the majority of these upregulated lncRNAs are newly synthesized.

To investigate whether the inhibition of nascent RNA production affects EZH2 chromatin occupancy and H3K27me3 deposition, we treated ACHN cells with DRB, a transcription inhibitor. The results indicated that as the concentration of DRB increased (leading to a stronger inhibition of nascent RNA production), both the chromatin binding level of EZH2 and the levels of H3K27me3 further increased (Supplementary Fig. S3C). This finding suggests that nascent RNA exerts an overall negative regulatory effect on the recruitment of EZH2 to chromatin.

To strongly support our conclusions, we conducted nascent RNA-seq to compare the transcriptional profiles of ACHN$^{ZCCHC8\text{-}WT}$ cells and *ACHN*$^{ZCCHC8\text{-}/-}$ cells. We utilized an emerging method known as SLAM-seq, employing 4-thiouridine (s4U) labeling and thiol group alkylation to differentiate and quantify nascent RNA from pre-existing RNA by detecting the conversion of thymine to cytosine (T > C) [55], a technique that is widely accepted in the field [60–62]. We treated both ACHN$^{ZCCHC8\text{-}WT}$ cells and ACHN$^{ZCCHC8\text{-}/-}$ cells with s^4U for 1 h, followed by alkylation and RNA-seq. The results from the SLAM-seq analysis indicated that ZCCHC8 deficiency resulted in the upregulation of a significant number of nascent lncRNAs, with a 2-fold increase in ACHN$^{ZCCHC8\text{-}/-}$ cells compared to ACHN$^{ZCCHC8\text{-}WT}$ cells (Fig. 3A). Feature distribution analysis showed that nearly half of these upregulated nascent lncRNAs were located on CpG islands (Fig. 3B), which are recognized as PRC2-enriched regions [63].

To further investigate whether the above upregulated nascent lncRNAs harbor specific regulatory motifs involved in the EZH2 chromatin recruitment, we analyzed their sequences using motif-based sequence analysis tools MEME. Previous PAR-CLIP-seq data have demonstrated that PRC2 preferentially binds to nascent RNAs, with tags for both EZH2 and JARID2 being more broadly enriched in the 5′ region of the transcript body [26]. Therefore, we focused our motif analysis on the 5′ region of upregulated nascent lncRNAs, which revealed a significant presence of G-rich sequences (commonly referred to as ‘G-tracts’) and U-rich sequences within these lncRNAs (Fig. 3C).

In mammals, PRC2 recognizes and binds G4 folded structures within single-stranded RNA. These interactions lead to the expulsion of the core catalytic component, EZH2, from the substrate nucleosome, ultimately resulting in a reduction of H3K27me3 levels in the gene [31, 64]. Additionally, analyses using various G4-structure prediction software (Fig. 3D) revealed that these G-rich sequences exhibited a high probability of folding into G4 structures. It is reported that the more consecutive ‘G’ in G-tracts and the higher the repetition of G-tracts, the greater possibility of forming G4 structures [64]. To comprehensively assess the potential of these upregulated nascent lncRNAs to form G4 structures, we further categorized these nascent lncRNAs into three types based on the predicted number of ‘G’ repetitions within their G-tracts sequences (Fig. 3E and Supplementary Fig. S3D). Among them:

Type I: 12.4% of upregulated nascent lncRNAs contained sequences with the $(G_{>3})_{1-2}$ $(G_2)_{0-5}$ feature, indicating the presence of 1–2 repeated G-tracts consisting of >3 repeated ‘G’, along with 0–5 repeated G-tracts consisting of 2 repeated ‘G’.

Type II: 54.2% of upregulated nascent lncRNAs harbored sequences with the $(G_{>3})_{3-5}$ $(G_2)_{0-3}$ feature, indicating the presence of 3–5 repeated G-tracts consisting of >3 repeated ‘G’, along with 0–3 repeated G-tracts consisting of 2 repeated ‘G’.

Type III: 33.4% of the upregulated nascent lncRNAs contained sequences that lacked the aforementioned features, suggesting they are unlikely to form a G4 structure (designated as G4-non).

Based on existing research on G4 structures, type II nascent lncRNAs are more likely to form G4 structures than type I.

Interestingly, U-Rich motifs were also significantly enriched in these upregulated nascent lncRNAs (Fig. 3C). Given that previous iCLIP-seq data have demonstrated the binding of the NEXT complex to U-Rich motifs via its subunit RBM7 [12], we hypothesized that these nascent lncRNAs containing U-Rich motifs might serve as targets for the NEXT complex, leading to their degradation within RNA exosomes. We classified nascent lncRNAs with >50% uridine (U) content within

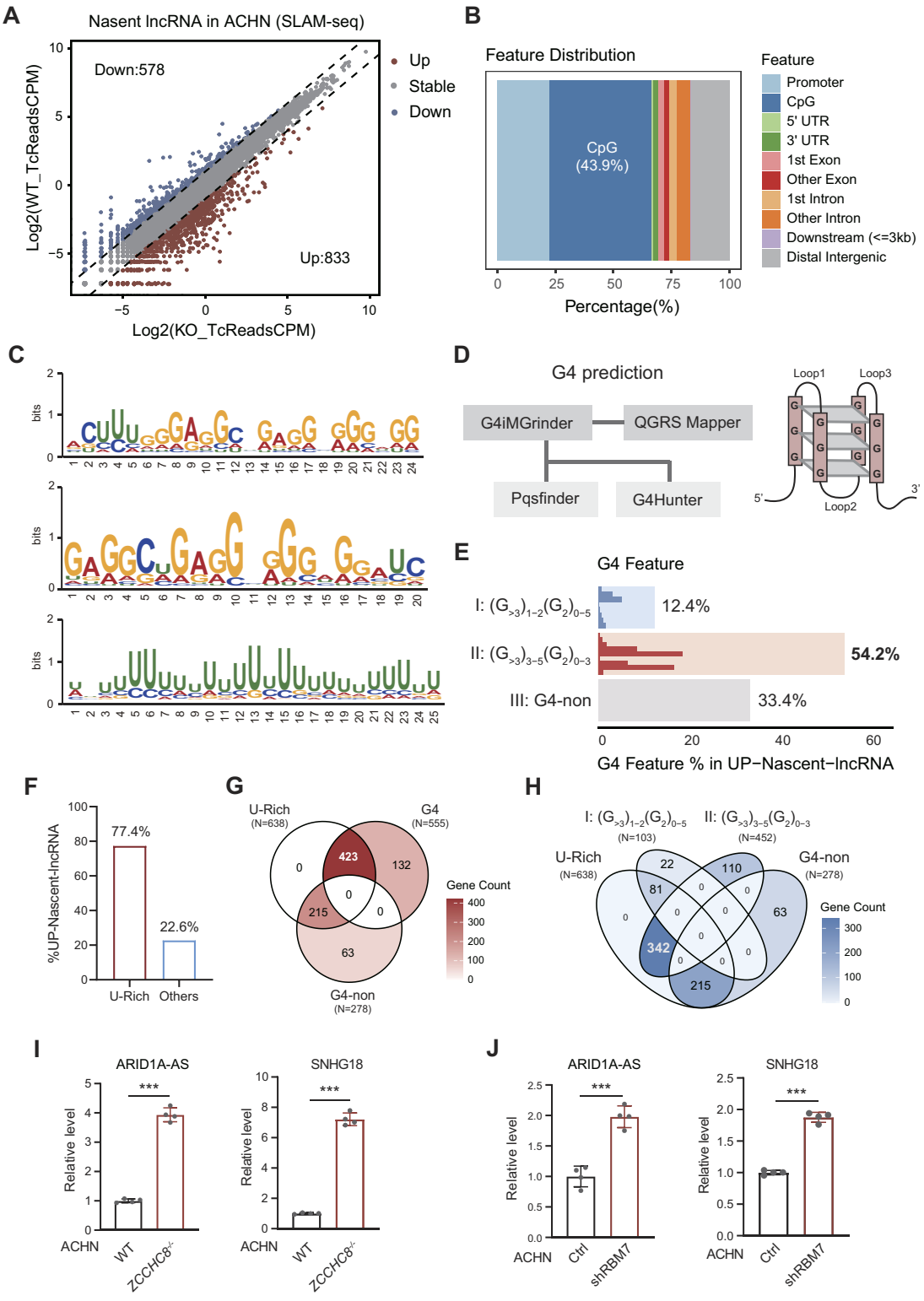

Figure 3. Impaired NEXT complex upregulates the levels of nascent G4/U-Rich lncRNAs. (**A**) Scatter plot for differentially expressed nascent lncRNAs (detected in SLAM-seq based on T > C conversions) in ACHN$^{ZCCHC8-/-}$ cells labeled with s^4U for 1 h. After excluding nascent lncRNAs with an average CPM value less than 1, the nascent lncRNAs whose TcReadsCPM changed by at least 2 folds were analyzed in the ACHN$^{ZCCHC8-/-}$ group compared to ACHN$^{ZCCHC8-WT}$ group. (**B**) Feature distribution analysis of upregulated nascent lncRNAs through R package Chipseeker. (**C**) MEME analysis revealed that upregulated nascent lncRNAs in ACHN$^{ZCCHC8-/-}$ cells were significantly enriched for G-Rich and U-Rich motifs. (**D**) Nascent lncRNAs were further predicted for G4s using multiple G4 prediction software and algorithms. (**E**) The proportion of upregulated nascent lncRNAs containing different G4 features was statistically analyzed. (**F**) The proportion of upregulated nascent lncRNAs containing U-Rich motif (defined as with >50% uridine in the 25 nt motifs) was statistically analyzed. (**G**) Venn diagram showed the intersection of nascent U-Rich-lncRNAs and nascent G4-containing lncRNAs. (**H**) Venn diagram showed the intersection of nascent U-Rich-lncRNAs and nascent lncRNAs containing different G4 types. (**I**, **J**) qPCR analyses for the levels of lncRNAs ARID1A-AS (left) and SNHG18 (right) in ACHN$^{ZCCHC8-/-}$ cells (**I**), as well as in ACHN-shRBM7 cells (**J**). Data were presented as mean ± SD, $n = 4$. Statistical analysis was performed using two-tailed unpaired *t*-test, $^{***}P < .001$.

25-nucleotide (nt) motifs as 'nascent U-Rich-lncRNAs'. Notably, 77.4% of the upregulated nascent lncRNAs fell into this category (Fig. 3F). Additionally, about 66.3% (423 out of 638) of these nascent U-Rich-lncRNAs also contained G4 sequences, with a majority exhibiting type II G4 structures (Fig. 3G and H). Furthermore, 76.2% (423 out of 555) of the nascent lncRNAs containing G4 structures also exhibited U-rich motifs, while 75.7% (342 out of 452) of the nascent lncRNAs with Type II G4 structures also harbored U-rich motifs simultaneously.

The G4 sequences within nascent lncRNAs were identified based on a high probability of forming G4 structures, taking into account G score and G4 characteristics (Supplementary Fig. S3E). Furthermore, the U-Rich sequences within the same lncRNAs were also identified (Supplementary Fig. S3E). Consequently, we collectively designated these nascent lncRNAs containing both G4 and U-Rich motifs as 'nascent G4/U-Rich lncRNAs'. Among these, ARID1A-AS and SNHG18 were chosen for validation of the sequencing results due to their high rankings. The results showed that both lncRNAs were significantly increased in ACHN$^{ZCCHC8-/-}$ cells (Fig. 3I). Given that RBM7 is essential for NEXT-mediated RNA decay [4], we generated an RBM7-knockdown ACHN cell line (ACHN-shRBM7) to confirm that they are substrates of the NEXT complex. Similar to the effect of ZCCHC8 KO/knockdown, RBM7 knockdown also led to a significant increase in ARID1A-AS and SNHG18 levels (Fig. 3J). Taken together, above data suggest that the impaired NEXT complex leads to a substantial upregulation of numerous nascent G4/U-rich lncRNAs.

Nascent **G4/U-Rich lncRNA directly binds to EZH2 and RBM7 via its G4 and U-Rich motif, respectively**

To validate whether those nascent G4/U-Rich lncRNAs indeed mediate the regulation of EZH2 recruitment by the NEXT complex, we conducted an RIP assay and showed that EZH2 could interact with both ARID1A-AS (Fig. 4A and Supplementary Fig. S4A) and SNHG18 (Fig. 4B and Supplementary Fig. S4B). To further investigate whether this interaction depends on the G4 structure, we mutated the predicated G4 sequences in ARID1A-AS and SNHG18 (Supplementary Fig. S3F). Subsequent RIP experiments showed that when the 'Gs' in the G4 sequence were mutated to 'As', the binding ability between EZH2 and ARID1A-AS (Fig. 4C and Supplementary Fig. S4C) or SNHG18 (Fig. 4D and Supplementary Fig. S4D) was significantly reduced, indicating that the interactions relied on their G4 structures. The electrophoretic mobility shift assay (EMSA) further confirmed the above conclusion. Specifically, bacterially expressed GST-EZH2 protein was purified and G4 structure sequences of ARID1A-AS and SNHG18 labeled with biotin at 5′- end were synthesized (Supplementary Fig. S3F). We observed that in RNA renaturation buffer containing K^+ that G4 structure can be formed, ARID1A-AS-bio-G4 could bind to GST-EZH2, and the binding strength enhanced with the increase of GST-EZH2 concentration (Fig. 4E). In contrast, in the RNA renaturation buffer containing Li^+ that G4 structure could not be formed, ARID1A-AS-bio-G4 failed to bind to EZH2 (Fig. 4E). Similarly, the G4 structure of SNHG18 directly bound to GST-EZH2 (Supplementary Fig. S4E). These results indicate that upregulated nascent G4/U-Rich lncRNAs such as ARID1A-AS and SNHG18 bind to EZH2 through their G4 structures, thereby hindering the binding of EZH2 to the chromatin and leading to a decrease in H3K27me3 levels at target gene loci.

To confirm whether upregulated nascent G4/U-Rich lncRNAs were recognized by RBM7 through U-Rich motifs, lysates from 293T cells overexpressing ARID1A-AS or SNHG18 were used for RIP with anti-RBM7 antibody. The results showed that RBM7 had very strong interactions with ARID1A-AS (Fig. 4F and Supplementary Fig. S4F) and SNHG18 (Fig. 4G and Supplementary Fig. S4G). Furthermore, we synthesized the U-Rich sequence of ARID1A-AS labeled with biotin at 5′-end (Supplementary Fig. S3F) for EMSA experiments. The results showed a direct interaction between RBM7 and the U-Rich sequence of ARID1A-AS (Fig. 4H).

As a member of the CCHC-type zinc finger protein family, ZCCHC8 also possesses RNA binding ability, especially to single-stranded RNA [65]. Studies have found that the CCHC-box domain (also known as the "ZnK" domain) of ZCCHC-type zinc finger proteins can recognize and bind to Gs in single-stranded RNA [66]. To further confirm whether upregulated nascent G4-lncRNAs were recognized by the NEXT complex through the RBM7/U-Rich interaction or the ZCCHC8/G-Rich interaction, we constructed two mutants of ZCCHC8: ZCCHC8-L295/299E and ZCCHC8-ΔZnK. The former involves mutating the L295 and L299 residues, which are essential for the interaction between ZCCHC8 and RBM7, to glutamic acid, thereby disrupting their interaction (Supplementary Fig. S4H). The latter involves deleting the ZnK domain of ZCCHC8, which results in the loss of its ability to bind to G-rich sequences in single-stranded RNA; however, this deletion does not impact the interaction between ZCCHC8 and RBM7 (Supplementary Fig. S4H). Subsequently, we assessed whether the bindings of these two ZCCHC8 mutants with lncRNAs are influenced. The RIP assays revealed that compared to ZCCHC8-WT, the binding ability of ZCCHC8-ΔZnK to ARID1A-AS was not affected (Fig. 4I and Supplementary Fig. S4I), and even the binding ability to SNHG18 was increased (Supplementary Fig. S4J), while the binding abilities of ZCCHC8-L295/299E to ARID1A-AS and SNHG18 were significantly reduced (Fig. 4I and Supplementary Fig. S4J). These findings suggested that ARID1A-AS and SNHG18 were targeted by the NEXT complex through the RBM7/U-Rich interaction. Collectively, the above results demonstrate that each of the upregulated nascent G4/U-Rich lncRNAs (such as ARID1A-AS and SNHG18) exhibits two characteristic structures. The G4 structure is responsible for binding to EZH2, while the U-Rich motif is specifically recognized by RBM7 and subsequently recruited into RNA exosomes for degradation (Fig. 4J).

In addition to ZCCHC8, RBM7, as another key component of the NEXT complex, was knocked down in ACHN and H1299 cells, revealing a significant decrease in H3K27me3 levels (Fig. 4K) without affecting the protein levels of the PRC2 core subunits (Supplementary Fig. S4K). To further confirm the essential role of the NEXT complex mediated RNA decay in regulating H3K27me3 levels, a core subunit of RNA exosomes, RRP40, was knocked down in ACHN and H1299 cells. Convincingly, knockdown of RRP40 indeed led to a significant decrease in H3K27me3 levels (Fig. 4L); Similarly, the reduction of RRP40 did not affect the expression levels of the PRC2 core subunits (Supplementary Fig. S4L).

Collectively, the above evidence supports a model in which U-Rich motifs within nascent G4/U-Rich lncRNAs are

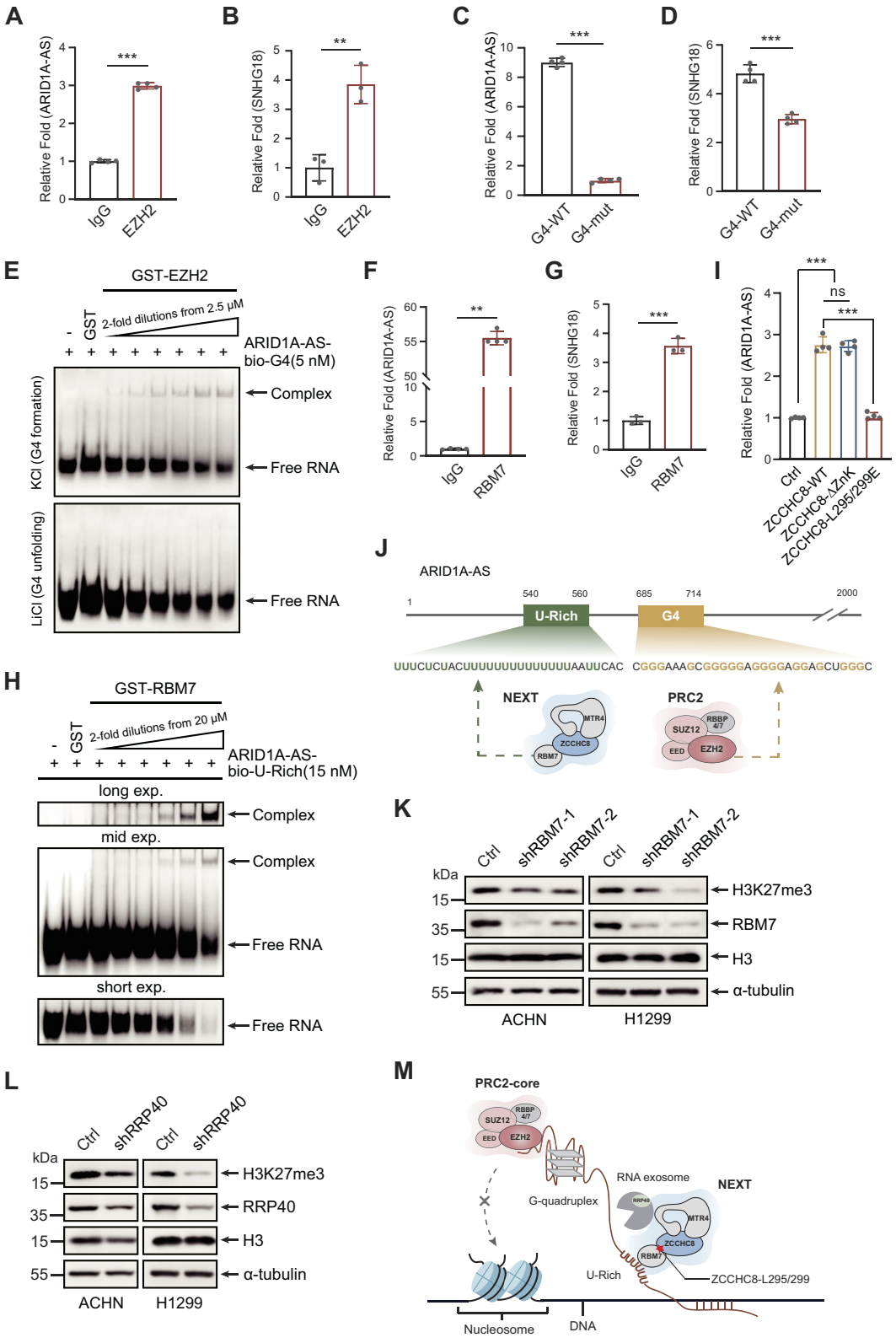

Figure 4. Nascent G4/U-Rich lncRNA directly binds to EZH2 and RBM7 via its G4 and U-Rich motif, respectively. (**A,B**) The RIP experiments were conducted to detect the binding between EZH2 and ARID1A-AS (**A**) as well as SNHG18 (**B**). Data were presented as mean ± SD, $n = 3$ or 4. Statistical analysis was performed using two-tailed unpaired *t*-test, $^{**}P < .01$, $^{***}P < .001$. (**C,D**)The RIP experiments were conducted to determine the binding between EZH2 and G4 sequence mutant of ARID1A-AS (**C**) as well as G4 sequence mutant of SNHG18 (**D**), $n = 4$, $^{***}P < .001$. (**E**) The EMSA experiment was performed to detect the direct interaction between GST-EZH2 and the G4-predicted sequence of ARID1A-AS. KCl promotes G4 formation, whereas LiCl inhibits it. (**F,G**) The RIP experiments were conducted to detect the binding between RBM7 and ARID1A-AS (**F**) as well as SNHG18 (**G**), $n = 3$ or 4, $^{**}P < .01$, $^{***}P < .001$. (**H**) EMSA experiments showed that RBM7 bound to the U-Rich sequence of ARID1A-AS. (**I**) RIP assays for the binding of ZCCCH8-WT, −ΔZnK, and −L295/299E to ARID1A-AS, $n = 4$, ns: $P \geq .05$, $^{***}P < .001$. (**J**) Schematic diagram of U-Rich sequence and G4 sequence in ARID1A-AS. (**K,L**) Western blotting analysis for H3K27me3 levels in ACHN and H1299 cell lines after knocking down RBM7 (**K**) and RRP40 (**L**). (**M**) A model of nascent lncRNAs interacting with complexes PRC2 and NEXT via G4 and U-Rich motif, respectively.

recognized by ZCCHC8/RBM7, components of the NEXT complex. Subsequently, these lncRNAs are recruited into exosomes for degradation. When the function of the NEXT complex is impaired, it disrupts the normal degradation of nascent G4/U-Rich lncRNAs, causing their accumulation in the nucleus. Consequently, the accumulated lncRNAs bind to EZH2, preventing the recruitment of PRC2 to the chromatin and resulting in low levels of H3K27me3 (Fig. 4M).

Upregulated nascent G4/U-Rich lncRNAs increase the expression levels of their neighboring genes

Since accumulated nascent G4/U-Rich lncRNAs bound to EZH2 through its G4 structure, thereby blocking the recruitment of EZH2 to the target loci for H3K27me3 marking, we further analyzed the ChIP sequencing data to evaluate the changes of H3K27me3 and EZH2 signals in genes adjacent to upregulated nascent G4/U-Rich lncRNAs. The results showed that both H3K27me3 and EZH2 signals were generally reduced at most adjacent gene loci in ACHN$^{ZCCHC8-/-}$ cells compared with ACHN$^{ZCCHC8\text{-}WT}$ cells (Fig. 5A and B). Next, we further analyzed the mRNA expression profiles from the SLAM-seq data, revealing that more mRNAs were upregulated in the absence of ZCCHC8 (Supplementary Fig. S5A). Notably, for most of the genes adjacent to the upregulated nascent lncRNAs, mRNA expression levels were elevated in ACHN$^{ZCCHC8-/-}$ cells (Fig. 5C). Interestingly, when compared to G4-non (type III) nascent lncRNAs, those nascent lncRNAs that contain G4 sequences showed a more significant increase in the expression of their adjacent genes, both at the levels of newly synthesized mRNA and total mRNA, which further supports our conclusions (Fig. 5D). Genome visualization using representative genome browser tracks provided detailed information on the ChIP signals for H3K27me3 and EZH2, along with the RNA expression levels of the lncRNA SNHG18 and its neighboring gene SEMA5A in *ZCCHC8*^{WT} and *ZCCHC8*$^{-/-}$ cells (Fig. 5E).

To validate the conclusions drawn from above ChIP-sequencing data, we conducted ChIP-qPCR assays to confirm that the levels of H3K27me3 and the binding affinity of EZH2 to the promoters of the neighboring genes SEMA5A (associated with SNHG18) and ARID1A (associated with ARID1A-AS) were significantly reduced in ACHN$^{ZCCHC8-/-}$ cells (Fig. 5F and Supplementary Fig. S5B). Consistent results were also observed in murine embryonic stem cell CGR8 with stable knockdown of ZCCHC8 (Fig. 5G and Supplementary Fig. S5C). Additionally, as expected, the mRNA levels of *SEMA5A* and *ARID1A* were significantly increased after ZCCHC8 KO in ACHN cells (Fig. 5H and Supplementary Fig. S5D).

Moreover, we overexpressed G4-containing lncRNA to examine its effects on both global and local levels of H3K27me3. The results indicated that the overexpression of SNHG18 (Supplementary Fig. S5F) or ARID1A-AS (Supplementary Fig. S5H) resulted in a reduction of global H3K27me3 levels (Supplementary Fig. S5E and G) in both ACHN and 293T cells or both ACHN and H1299 cells, respectively. Notably, both H3K27me3 and EZH2 signals at the promoter of the neighboring gene of SNHG18, *SEMA5A*, were significantly diminished when SNHG18 was overexpressed in ACHN cells (Fig. 5I). Conversely, in cells expressing the mutant SNHG18-G4-mut, the H3K27me3 and EZH2 signals at the chromatin were restored (Fig. 5I).

It is reported that mammalian PRC2 binding sites are enriched in CG content, which correlate with CpG islands that display a low level of DNA methylation [67]. The gene sets, denoted as 'HCP with H3K27me3' and 'LCP with H3K27me3' (Supplementary Fig. S5I), comprise genes bearing H3K27me3 mark in the high-CpG-density promoters (HCP) and low-CpG-density promoters (LCP), respectively. GSEA analysis revealed that genes in HCP gene set were significantly enriched in ACHN$^{ZCCHC8-/-}$ cells, while genes in LCP gene set were significantly enriched in ZCCHC8-WT cells (Supplementary Fig. S5I). This indicated that ZCCHC8 KO resulted in the upregulation of genes in HCP gene set and the downregulation of genes in LCP gene set, implying a positive correlation between the levels of ZCCHC8 and H3K27me3. Thus, the above results demonstrate that upregulated nascent G4/U-Rich lncRNAs in ACHN$^{ZCCHC8-/-}$ cell lines enhance the transcriptional activity of their neighboring genes by decreasing the levels of H3K27me3 on their promoters, thereby increasing the mRNA levels of neighboring genes.

ZCCHC8 is identified as a new oncogene

By conducting Gene Ontology (GO) pathway enrichment analysis on neighboring genes of upregulated nascent lncRNAs, we observed significant enrichment in several pathways, including angiogenesis, mesenchymal cell differentiation, epithelial cell migration, and epithelial-to-mesenchymal transition, following ZCCHC8 KO (Supplementary Fig. S6A). These findings implied that ZCCHC8 might contribute to cancer progression by modulating signaling pathways associated with tumor cell migration. Indeed, analyses on protein quantification mass spectrometry data from the Clinical Proteomic Tumor Analysis Consortium (CPTAC) database unveiled a marked elevation in ZCCHC8 protein levels across several malignant tumors, including ccRCC, LUAD, hepatocellular carcinoma, breast cancer, and ovarian cancer, when compared to their corresponding normal adjacent tissues (Fig. 6A). Considering individual differences among patients, we paired tumor tissues and their corresponding adjacent tissues from the same ccRCC and LUAD patients (the data from CPTAC), and then compared the differences in ZCCHC8 protein levels, arriving at the same conclusion that ZCCHC8 was highly expressed in tumors (Supplementary Fig. S6B). Furthermore, as tumor pathological grading increased, the proportion of patients with high expression of ZCCHC8 also showed a gradual rise (Fig. 6B). Similarly, upon analyzing the expression levels of ZCCHC8 in patients with varying pathological grades, we observed a consistent increasing trend as the pathological grade advanced (Supplementary Fig. S6C). Thus, based on the data from CPTAC, the analysis revealed a significant positive correlation between the expression level of ZCCHC8 and tumor grade, particularly in LUAD and ccRCC patients. Furthermore, the Kaplan–Meier survival analysis showed that patients with high mRNA expression levels of ZCCHC8 exhibited a lower survival rate in both ccRCC and LUAD patients (Fig. 6C and D), which suggests a positive correlation between ZCCHC8 overexpression and an unfavorable prognosis in patients.

To validate the aforementioned conclusions derived from public databases, we conducted western blotting analysis to evaluate the protein levels of ZCCHC8 in clinical tumor specimens and their corresponding adjacent normal

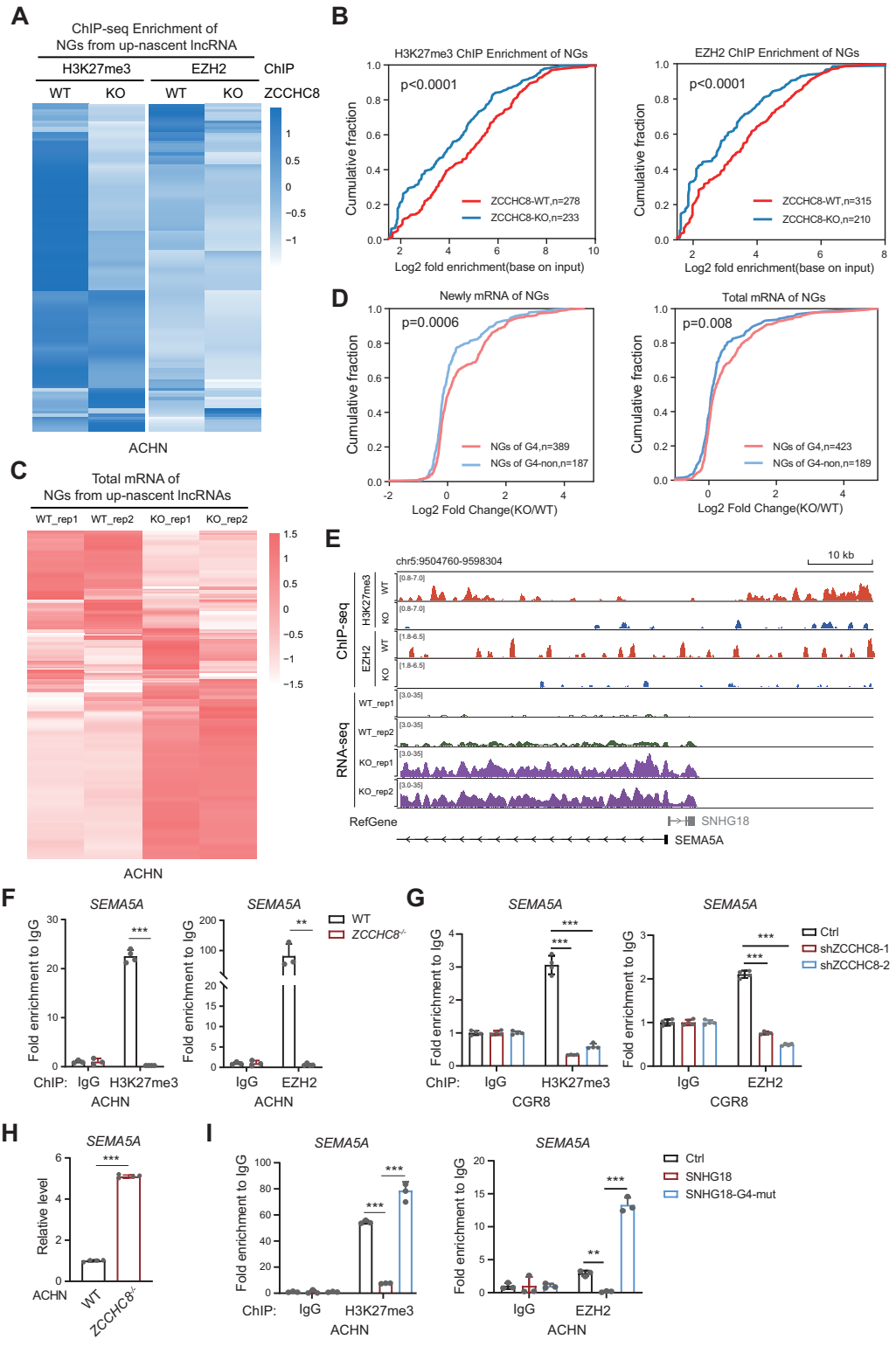

Figure 5. Upregulated nascent G4/U-Rich lncRNAs enhance the expression levels of their neighboring genes. (**A**) Heatmap showed differential enrichment of H3K27me3-ChIP-seq and EZH2-ChIP-seq peaks in the proximate genes of all upregulated nascent lncRNAs in ACHN$^{ZCCHC8-/-}$ cells compared to ACHN$^{ZCCHC8\text{-}WT}$ cells. (**B**) Cumulative distribution plots showed the differential enrichment of H3K27me3-ChIP-seq (left) and EZH2-ChIP-seq (right) peaks in the proximate genes of all upregulated nascent lncRNAs in ACHN$^{ZCCHC8-/-}$ cells compared to ACHN$^{ZCCHC8\text{-}WT}$ cells. (**C**) Heatmap showed the mRNA expression profile of adjacent genes form upregulated nascent lncRNAs. (**D**) Cumulative distribution plots showed the changes in the levels of newly generated mRNAs and total mRNAs of neighboring genes from upregulated nascent lncRNAs with or without G4 sequences. (**E**) Representative genome browser tracks for signal peaks of H3K27me3 and EZH2 (ChIP-seq), and RNA levels of SNHG18 and its proximate gene *SEMA5A* (RNA-seq) in ACHN$^{ZCCHC8\text{-}WT}$ and ACHN$^{ZCCHC8-/-}$ cells. (**F,G**) ChIP-qPCR experiments were performed to detect the levels of H3K27me3 and EZH2 binding to SEMA5A promoter in ACHN$^{ZCCHC8-/-}$ cells (**F**) and ZCCHC8-knockdown CGR8 cells (**G**), $n = 3$ or 4, $^{***}P < .001$, $^{**}P < .01$. (**H**) The expression levels of *SEMA5A* in ACHN$^{ZCCHC8-/-}$ cells were determined by qPCR, $n = 4$, $^{***}P < .001$. (**I**) ChIP-qPCR for the levels of H3K27me3 and EZH2 binding to SEMA5A promoter in ACHN cells overexpressing SNHG18 with wild-type G4 sequence or G4-mutanted sequence, $n = 3$, $^{***}P < .001$, $^{**}P < .01$.

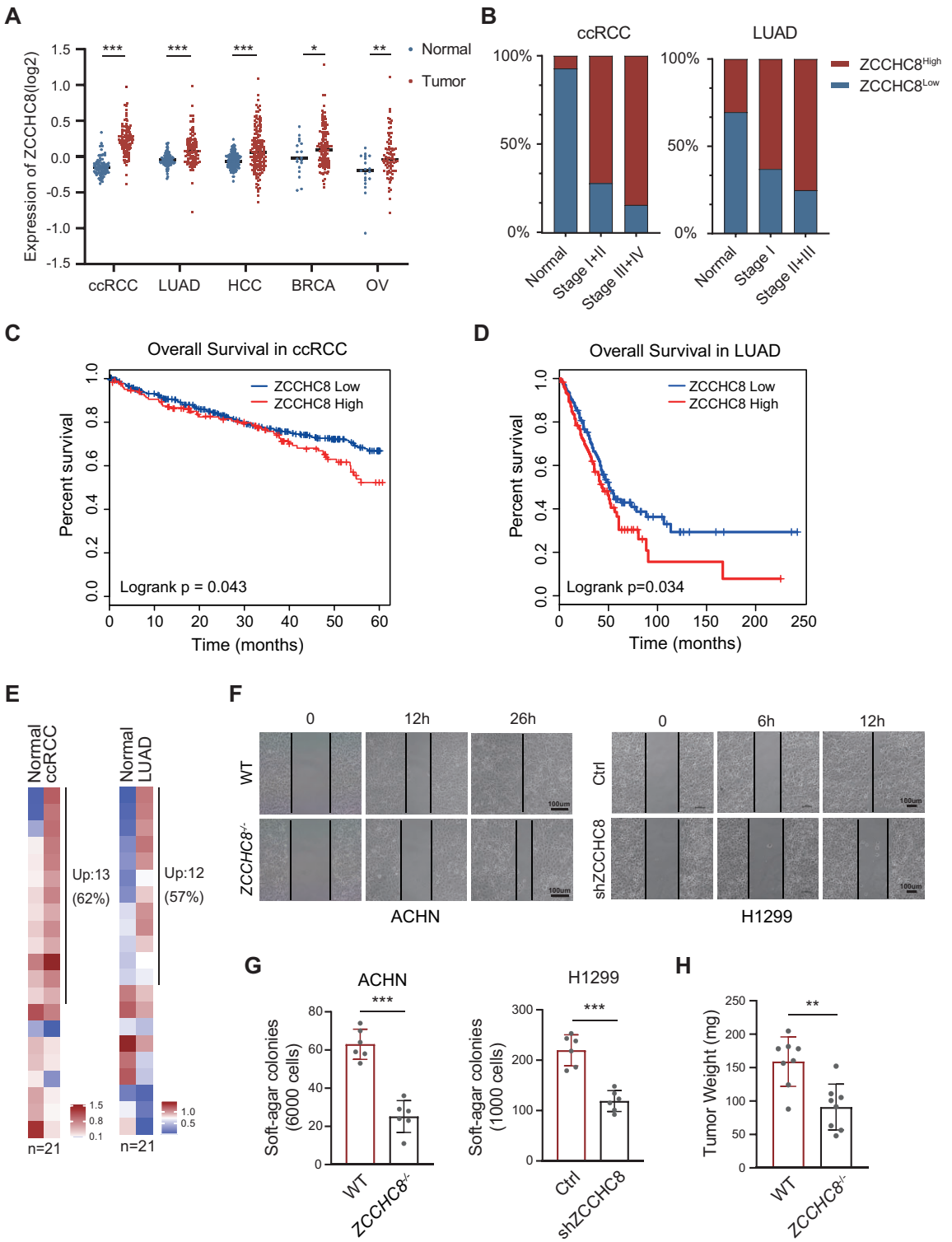

Figure 6. ZCCHC8 promotes cancer progression. (**A**, **B**) Analysis of ZCCHC8 protein levels in the public database of Clinical Proteomic Tumor Analysis Consortium (CPTAC). The protein level of ZCCHC8 was higher in tumor tissues compared to adjacent normal tissues (**A**), and the proportion of patients with high ZCCHC8 expression increased with the rise in pathological grade in ccRCC and LUAD patients (**B**). Statistical analysis was performed using two-tailed unpaired *t*-test in panel (A), $***P < .001$, $**P < .01$, $*P < .05$. (**C,D**) The correlations between the mRNA expression level of ZCCHC8 and the survival of ccRCC patients (**C**) as well as LUAD patients (**D**) were analyzed by the online tool Kaplan–Meier plotter and compared by the log-rank test. (**E**) Expression levels of ZCCHC8 in ccRCC and LUAD clinical specimens as well as their paired adjacent normal tissues (21 pairs, respectively) were analyzed by western blotting. Heatmap was used to display the results of grayscale statistics. (**F**) KO or knockdown of ZCCHC8 levels inhibited the wound healing ability of ACHN (left) and H1299 (right) cells. (**G**) Soft agar colony formation assay for stable ACHN (left) and H1299 (right) cells were performed according to the 'Materials and methods' section. Data were presented a mean ± SD, $n = 6$. Statistical analysis was performed using two-tailed unpaired t-test. $***P < .001$. (**H**) Stable ACHN cells were subcutaneously injected into 6-week-old BALB/c nude mice individually (2.5×10^6 cells per each). Mice were sacrificed after 3 weeks of injection. Tumors were dissected and the weight was assessed. Data were presented as mean ± SD, $n = 8$. Statistical analysis was performed using two-tailed unpaired *t*-test. $**P < .01$.

tissues from 21 ccRCC and LUAD patients, respectively (see Supplementary Table S3). As anticipated, the results revealed that ZCCHC8 levels were generally higher in tumors compared to those in adjacent normal tissues (Fig. 6E and Supplementary Fig. S6D). Secondly, we performed a wound healing assay and observed a marked decrease in the healing capacity of ccRCC cell line ACHN, as well as LUAD cell line H1299, following ZCCHC8 KO or knockdown (Fig. 6F and Supplementary Fig. S6E). Notably, ZCCHC8 did not influence cell proliferation, effectively ruling out any impact of proliferation on migration (Supplementary Fig. S6F). Third, to investigate the impact of ZCCHC8 on cell transforming potential, we conducted a soft-agar colony-forming assay, which revealed that ZCCHC8 deletion or knockdown significantly reduced anchorage-independent colony formation and growth in ACHN and H1299 cells (Fig. 6G and Supplementary Fig. S6G). Furthermore, to investigate whether higher expression of ZCCHC8 promotes tumor growth *in vivo*, stable ACHN cell lines were subcutaneously inoculated into the backs of nude mice for the xenograft tumor growth assay. The photographs (Supplementary Fig. S6H) were taken, and the weight of tumors (Fig. 6H) was measured. The protein levels of ZCCHC8 in each of tumor tissues were verified by western blotting (Supplementary Fig. S6I). The results showed that the size and average weight of tumors in the ACHN$^{ZCCHC8-/-}$ group were reduced compared to those in the ACHN$^{ZCCHC8-WT}$ group, demonstrating that ZCCHC8 deletion inhibits tumor growth *in vivo*. Taken together, our data collectively demonstrate that ZCCHC8 functions as an oncogene, potentially contributing to both tumorigenesis and cancer progression.

ZCCHC8 promotes cancer progression by downregulating the expressions of SEMA5A and ARID1A

SEMA5A is a member of the semaphorin family and plays a crucial role in axon guidance. One study has demonstrated that SEMA5A functions as a tumor suppressor, inhibiting the proliferation and migration of LUAD cells [40]. However, in the context of pancreatic cancer and gastric cancer, SEMA5A seems to promote metastasis by enhancing endothelial cell proliferation and inhibiting apoptosis [68, 69]. ARID1A, a member of the SWI/SNF (Switch/Sucrose Non-Fermentable) chromatin-remodeling complex, plays a crucial role in regulating various biological processes, including cell differentiation, proliferation, development, and DNA repair [70]. Frequent mutations in the ARID1A gene occur in cancer, often involving insertions or deletions. These mutations lead to downregulation or loss of ARID1A protein expression [71]. Emerging evidence suggests that the loss of ARID1A significantly contributes to the development of several types of cancer, including colorectal cancer, gastric cancer, endometrial cancer, and cholangiocarcinoma [72, 73].

To explore whether ZCCHC8 overexpression (Fig. 6A–E and Supplementary Fig. S6B and C) in cancer patients results in decreased expression levels of the above neighboring SEMA5A and ARID1A, we conducted a comprehensive analysis of SEMA5A and ARID1A levels in clinical tumor tissues. Notably, the mRNA levels of SEMA5A and ARID1A were significantly reduced in kidney cancer and LUAD tissues compared to their corresponding normal adjacent tissues (Supplementary Fig. S7A–C). Furthermore, SEMA5A protein levels were also significantly decreased in kidney cancer and LUAD tissues (Fig. 7A and B). Subsequently, we performed correlation analyses, revealing that the protein levels of ZCCHC8 were negatively correlated with the mRNA levels of SEMA5A and ARID1A (Supplementary Fig. S7D–F). Most notably, the protein levels of SEMA5A also exhibited a negative correlation with the protein levels of ZCCHC8 in kidney and lung tissues (Fig. 7C and D).

Given the negative correlation between SEMA5A and ZCCHC8 at both mRNA and protein levels, we further investigated whether the phenotype resulting from ZCCHC8 KO is associated with SEMA5A. Elevated SEMA5A expression in ACHN$^{ZCCHC8-/-}$ cells was stably re-knocked down using lentiviral shRNA (Supplementary Fig. S7G). The wound healing assay revealed that the migration capacity of ACHN$^{ZCCHC8-/-}$ cells, which had been impaired due to ZCCHC8 KO, was rescued upon SEMA5A knockdown (Fig. 7E). Furthermore, the plate and soft-agar colony formation assays demonstrated that after SEMA5A knockdown, the proliferation capacity and the anchorage-independent growth ability of ACHN$^{ZCCHC8-/-}$ cells also were recovered nearly to wild-type levels, respectively (Fig. 7F and G, and Supplementary Fig. S7H and I). These intriguing findings lend support to our hypothesis that ZCCHC8 regulates SNHG18 levels through the NEXT complex, ultimately influencing the expression of its neighboring gene, SEMA5A, and thereby impacting cancer progression.

Cancer cells with high expression of ZCCHC8 are more sensitive to the EZH2 inhibitor

Dysregulation of the PRC2 complex is commonly observed in multiple cancers, particularly involving the catalytic subunit EZH2, which is frequently overexpressed or exhibits enhanced activity [74]. Tazemetostat (EPZ-6438) is an orally administered, first-in-class, small molecule EZH2 inhibitor that has been approved for clinical therapy [37]. Based on our aforementioned findings, we speculated that the EZH2 inhibitor might enhance the therapeutic efficacy in cancer patients with high expression of ZCCHC8. To validate this hypothesis, we treated ZCCHC8-high expressed ACHN$^{ZCCHC8-WT}$ cells and ACHN$^{ZCCHC8-/-}$ cells with EPZ-6438. Subsequently, we measured the levels of H3K27me3 using western blotting. Notably, there was a significant decrease in H3K27me3 levels in ACHN $^{ZCCHC8-WT}$ cells compared to ACHN$^{ZCCHC8-/-}$ cells (Fig. 8A and B). This finding suggests that cancer cells with high expression of ZCCHC8 were more sensitive to EPZ-6438.

Given the substantial elevation in ZCCHC8 protein levels observed in ccRCC (Fig. 6A–E and Supplementary Fig. S6B–D), and considering that pazopanib is a frequently prescribed first-line drug for advanced ccRCC patients, we hypothesize that the combination of pazopanib and EPZ-6438 could synergistically enhance the therapeutic efficacy in ccRCC cases with high ZCCHC8 expression. We treated ACHN$^{ZCCHC8-WT}$ and ACHN$^{ZCCHC8-/-}$ cells with single-agent EPZ-6438 or pazopanib, as well as the combination of both. Cell viability was assessed using CCK8, revealing that the viability of ACHN$^{ZCCHC8-WT}$ cells decreased to below 50% when pazopanib and EPZ-6438 were combined, compared to the pazopanib group. However, the viability of ACHN$^{ZCCHC8-/-}$ cells did not exhibit further reduction (Fig. 8C). Similarly, in CAKI-1 and HK-2 cells with lower ZCCHC8 expression,

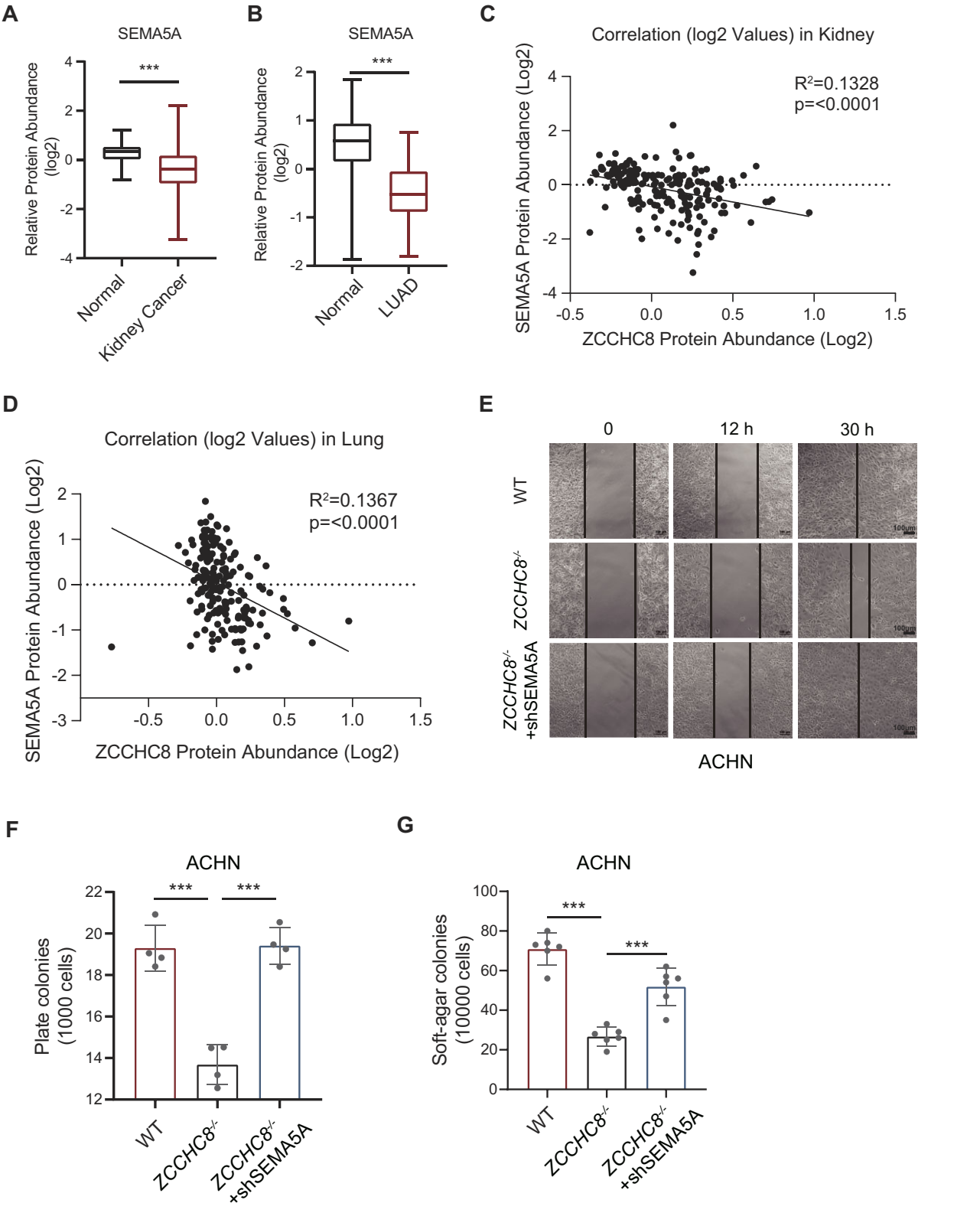

Figure 7. Neighboring genes SEMA5A and ARID1A are negatively correlated with ZCCHC8 levels in clinical cancer patients. (**A,B**) SEMA5A protein level in kidney cancer (**A**) and LUAD (**B**) were analyzed through Cancer Proteogenomic Data Analysis Site (cProSite). (**C,D**) Correlation between ZCCHC8 protein level and SEMA5A protein level in kidney (**C**) as well as lung (**D**) were analyzed by cProSite. (**E**) Knockdown of SEMA5A rescued the decreased cell migration ability caused by ZCCHC8 deficiency in ACHN cells. (**F**) Plate colony formation assay for ACHN stable cell lines were performed according to the 'Materials and methods' section. Data were presented a mean ± SD, $n = 4$. Statistical analysis was performed using one-way ANOVA. $^{***}P <$ .001. (**G**) Knockdown of SEMA5A rescued the decreased anchorage-independent growth capacity caused by ZCCHC8 deficiency. Data were presented a mean ± SD, $n = 6$. Statistical analysis was performed using one-way ANOVA. $^{***}P <$ .001.

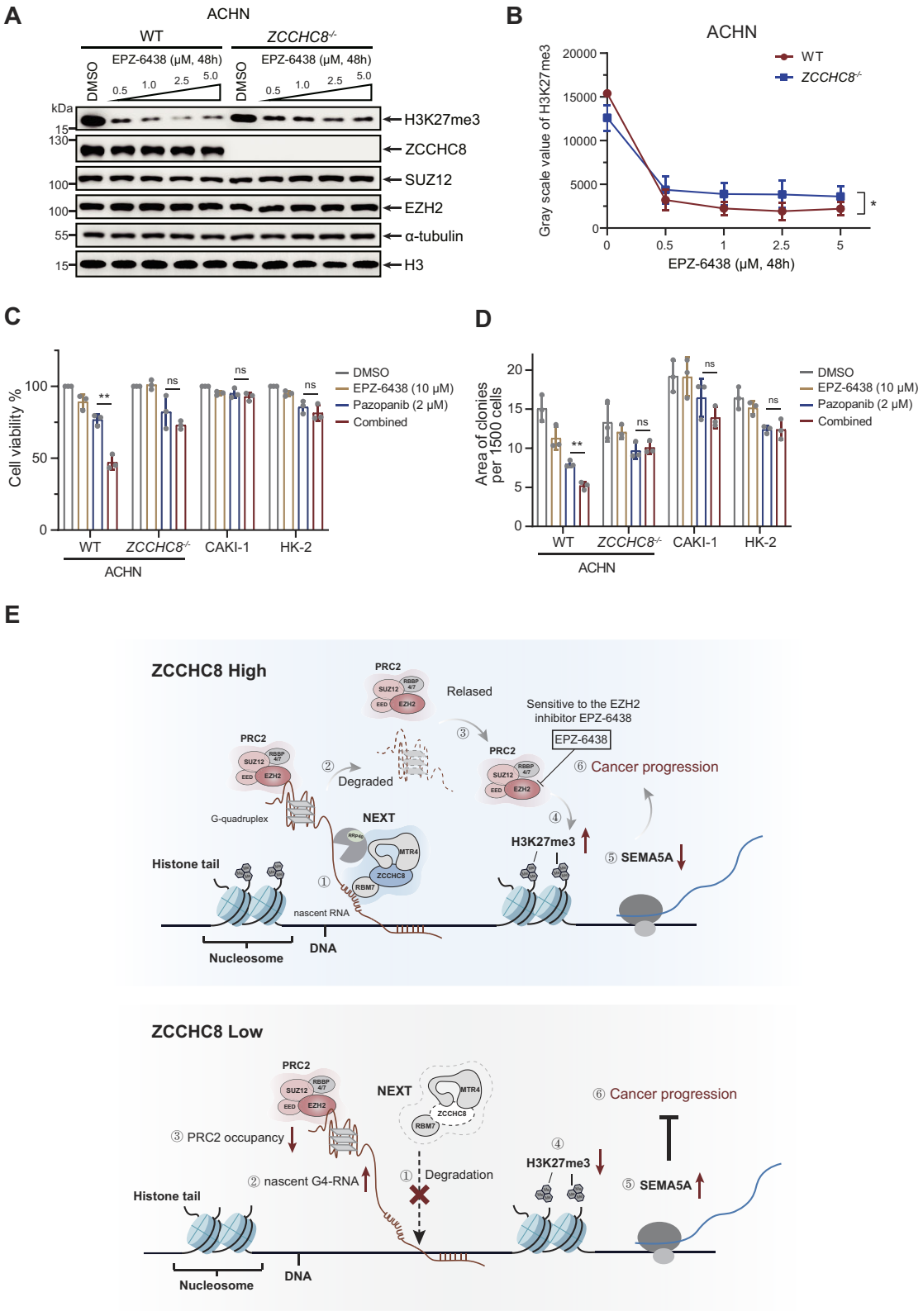

Figure 8. Cells with high ZCCHC8 expression are more sensitive to the EZH2 inhibitor EPZ-6438. (**A,B**) ACHN$^{ZCCHC8\text{-}WT}$ and ACHN$^{ZCCHC8\text{-}/-}$ cells were treated with different concentrations of EPZ-6438. After 48 h, the H3K27me3 levels were detected by western blotting (**A**), and quantified and normalized to H3 with Image J (**B**), $n = 3$, $^{*}P < .05$. (**C**) The cell viability was assessed using a CCK8 assay in ACHN$^{ZCCHC8\text{-}WT}$, ACHN$^{ZCCHC8\text{-}/-}$, CAKI-1, and HK-2 cells treated with EPZ-6438 or pazopanib alone and in combination,$n = 3$, ns: $P \geq .05$, $^{**}P < .01$. (**D**) EPZ-6438 or pazopanib treatment alone and in combination in cells (1500 cells/well) with fresh medium (containing the respective drugs) replaced every 3 days, crystal violet staining was performed after 2 weeks. Statistical analysis of the stained area was performed using two-tailed unpaired *t*-test, $n = 3$, ns: $P \geq .05$, $^{**}P < .01$. (**E**) The molecular mechanism by which ZCCHC8 regulates H3K27me3 involves an over-activated NEXT complex resulting from high expression of ZCCHC8. This over-activation leads to the excessive degradation of nascent G4/U-Rich lncRNAs, subsequently promoting increased recruitment of PRC2 and deposition of H3K27me3. Consequently, adjacent gene expression, such as SEMA5A, is inhibited, ultimately contributing to tumor progression (upper). Conversely, low ZCCHC8 expression inhibits tumor progression (lower).

the combination of pazopanib and EPZ-6438 also did not further promote cytotoxicity (Fig. 8C). This suggested that the combination of the EZH2 inhibitor EPZ-6438 could enhance the cytotoxicity of pazopanib on cells with high ZCCHC8 expression. Furthermore, plate colony formation assays further confirmed the above conclusion. The combination of pazopanib and EPZ-6438 demonstrated enhanced cytotoxic effects compared to the pazopanib monotherapy group in ACHN$^{ZCCHC8\text{-}WT}$ cells. However, ACHN$^{ZCCHC8\text{-}/-}$, CAKI-1, and HK-2 cell lines did not exhibit similar enhancement (Fig. 8D and Supplementary Fig. S8A).

Discussion

The initiation and progression of tumors result from the interplay between stable genetic variations and dynamic epigenetic changes in the genome. While most of the identified tumor-related genes, such as tumor suppressor genes or proto-oncogenes, lead to tumorigenesis through mutations in DNA sequences, much remains unknown about the associated epigenetic characteristics. Consequently, tumor epigenetics has become a hot research area, with promising insights emerging from recent studies. Polycomb group (PcG) proteins are epigenetic factors that form two main complexes known as Polycomb Repressive Complex 1 and 2 (PRC1 and PRC2). These complexes deposit H2AK119ub1 and H3K27me3, respectively. Most recently, a study has demonstrated that transient disturbances in transcriptional silencing mediated by polycomb group proteins are sufficient to induce irreversible changes in the fate of cells, even in the absence of mutations in driver genes [75]. H3K27me3 is a mark of facultative heterochromatin and gene silencing, often excessively modified in various cancers [76]. The PRC2 complex, as the only known multi-subunit complex with catalytic activity for H3K27me3, is directly associated with various cancers and developmental disorders when its function is disrupted [76, 77].

As noncoding RNA research advances, an increasing number of studies highlight the pivotal role of noncoding RNAs in epigenetic regulation. Among these, the NEXT complex stands out as an essential player responsible for RNA degradation and maintaining RNA stability. By orchestrating the degradation of nascent RNA, the NEXT complex actively participates in gene expression regulation. However, when the function of the NEXT complex is impaired, an imbalance in the steady-state of nascent lncRNAs ensues, leading to dysregulation in the transcriptional control of downstream genes. This dysregulation can significantly contribute to the onset of various diseases, particularly cancers. In our study, we uncovered functional connections between the NEXT complex and PRC2 complex, and proposed a specific molecular mechanism model (Fig. 8E). The nascent G4/U-Rich lncRNA serves as a critical regulator. Its G4 structure plays a pivotal role in facilitating EZH2 binding, which in turn blocks the chromatin recruitment of PRC2. Simultaneously, the U-Rich motif within this lncRNA is specifically recognized by RBM7/ZCCHC8 of the NEXT complex, leading to exosome-mediated RNA degradation. In tumor tissues with high ZCCHC8 expression, the function of the NEXT complex becomes excessively activated to degrade nascent G4/U-Rich lncRNAs via binding to its U-Rich motifs, thus core subunits of PRC2 (such as EZH2 and SUZ12) are released and easily recruited to neighboring genomic loci. This leads to an upregulation of H3K27me3 levels. Consequently, transcription at these adjacent gene loci is suppressed, including some tumor suppressor genes like SEMA5A and ARID1A, ultimately promoting tumor progression (Fig. 8E, upper). However, in normal tissues where ZCCHC8 expression is lower, the function of the NEXT complex is not excessively activated. As a consequence, these nascent lncRNAs can persistently reside within the cell nucleus, inhibiting the binding of PRC2 to nearby gene loci and thereby reducing H3K27me3 levels (Fig. 8E, lower).

We observed that in tumor cells, loss or downregulation of ZCCHC8, a key subunit of the NEXT complex, reduced the chromatin occupancy of EZH2, the catalytic subunit of PRC2. This reduction led to an overall decrease in H3K27me3 levels. RNA high-throughput sequencing analysis revealed that nascent lncRNA levels were significantly elevated in ACHN$^{ZCCHC8\text{-}/-}$ cells compared to ACHN$^{ZCCHC8\text{-}WT}$ cells, along with a corresponding increase in the expression of neighboring genes of these lncRNAs. Approximately 77.4% of upregulated nascent lncRNAs contained U-Rich motifs. Among the nascent lncRNAs with U-Rich motif, 66.3% also contained sequences that may form G4 structures. The U-Rich motifs could be recognized and bound by RBM7, another subunit of the NEXT complex, and were targeted to the RNA exosome for degradation as a substrate of the NEXT complex. The assembly and function of the NEXT complex were impaired due to loss or downregulation of ZCCHC8. Consequently, a portion of nascent G4/U-Rich lncRNAs accumulated in the nucleus due to blocked degradation. The abundant accumulation of G4 on nascent lncRNAs could directly bind to the catalytic subunit EZH2 of PRC2, thus inhibiting its binding on chromatin. This resulted in a decrease in H3K27me3 levels at adjacent loci of nascent G4/U-Rich lncRNAs, ultimately promoting the transcriptional activation of neighboring genes. Furthermore, GO analysis revealed that the neighboring genes of the upregulated lncRNAs in ACHN$^{ZCCHC8\text{-}/-}$ cells were significantly enriched in multiple pathways associated with tumor migration, which suggested that dysfunction of the NEXT complex might play a role in tumor progression. Subsequent cellular phenotype experiments and subcutaneous murine xenograft models demonstrated that the loss or downregulation of ZCCHC8 significantly inhibited the malignant phenotype of tumor cells, including their migration and *in vivo* tumorigenesis. More importantly, analysis of clinical cancer patient samples and international public clinical data revealed that ZCCHC8 protein levels in tumor tissues were significantly higher than those in adjacent noncancerous tissues. Conversely, the expression levels of target genes *SEME5A* and *ARID1A* were markedly lower in tumor tissues compared to adjacent noncancerous tissues, and exhibited a significant negative correlation with ZCCHC8 protein levels. Finally, the EZH2 inhibitor Tazemetostat (EPZ-6438) was found to enhance drug sensitivity in cells with elevated ZCCHC8 expression, suggesting a potential combination therapy strategy for cancer patients with increased ZCCHC8 levels. In summary, our study revealed a novel molecular mechanism by which the NEXT complex promotes H3K27me3 levels through the degradation of nascent G4/U-Rich lncRNAs.

Acknowledgements

Author contributions: Qianqian Yang: Conceptualization, Methodology, Investigation, Data Curation, Formal Analysis, Writing - Original Draft. Zihan Zhou, Lian Li, Runhui

Lu, Guofang Hou: Methodology, Investigation, Data Curation, Validation, Software, Visualization. Caihu Huang, Jiayi Huang, Hongyan Li, Yafan Zhang, Junya Li, Yixin Zhang, Anan Xu, Ran Chen, Yanli Wang, Xian Zhao, Jian Huang: Visualization, Investigation, Resources, Project Administration, Software. Yiwei Wang, Xiaojing Zhao: Resources, Conceptualization, Funding Acquisition. Jianxiu Yu: Conceptualization, Methodology, Funding Acquisition, Resources, Supervision, Project Administration, Writing - Review & Editing.

Supplementary data

Supplementary data is available at NAR online.

Conflict of interest

None declared.

Funding

National Natural Science Foundation of China [No. 82230100, 82273138, 32461160262, 32271310]. Funding to pay the Open Access publication charges for this article was provided by National Natural Science Foundation of China [No. 82230100].

Data availability

Uncropped immunoblot images for this article are included in the Supplementary Information. Source data are provided with this paper. All other data supporting the findings of the paper are available from the corresponding author upon reasonable request. All the raw data of high throughput sequencing are available from the Gene Expression Omnibus under accession code GSE243767 (for RNA-seq and ChIP-seq), and GSE284433 (for SLAM-seq).

References

1. Houseley J, LaCava J, Tollervey D. RNA-quality control by the exosome. *Nat Rev Mol Cell Biol* 2006;**7**:529–39. https://doi.org/10.1038/nrm1964
2. Wolin SL, Maquat LE. Cellular RNA surveillance in health and disease. *Science* 2019;**366**:822–7. https://doi.org/10.1126/science.aax2957
3. Kilchert C, Wittmann S, Vasiljeva L. The regulation and functions of the nuclear RNA exosome complex. *Nat Rev Mol Cell Biol* 2016;**17**:227–39. https://doi.org/10.1038/nrm.2015.15
4. Lubas M, Christensen MS, Kristiansen MS *et al.* Interaction profiling identifies the human nuclear exosome targeting complex. *Mol Cell* 2011;**43**:624–37. https://doi.org/10.1016/j.molcel.2011.06.028
5. Meola N, Domanski M, Karadoulama E *et al.* Identification of a nuclear exosome decay pathway for processed transcripts. *Mol Cell* 2016;**64**:520–33. https://doi.org/10.1016/j.molcel.2016.09.025
6. Ogami K, Richard P, Chen Y *et al.* An Mtr4/ZFC3H1 complex facilitates turnover of unstable nuclear RNAs to prevent their cytoplasmic transport and global translational repression. *Genes Dev* 2017;**31**:1257–71. https://doi.org/10.1101/gad.302604.117
7. Das M, Zattas D, Zinder JC *et al.* Substrate discrimination and quality control require each catalytic activity of TRAMP and the nuclear RNA exosome. *Proc Natl Acad Sci USA* 2021;**118**:e2024846118. https://doi.org/10.1073/pnas.2024846118
8. Puno MR, Lima CD. Structural basis for RNA surveillance by the human nuclear exosome targeting (NEXT) complex. *Cell* 2022;**185**:2132–47. https://doi.org/10.1016/j.cell.2022.04.016
9. Preker P, Nielsen J, Kammler S *et al.* RNA exosome depletion reveals transcription upstream of active human promoters. *Science* 2008;**322**:1851–4. https://doi.org/10.1126/science.1164096
10. Gable DL, Gaysinskaya V, Atik CC *et al.* ZCCHC8, the nuclear exosome targeting component, is mutated in familial pulmonary fibrosis and is required for telomerase RNA maturation. *Genes Dev* 2019;**33**:1381–96. https://doi.org/10.1101/gad.326785.119
11. Hrossova D, Sikorsky T, Potesil D *et al.* RBM7 subunit of the NEXT complex binds U-rich sequences and targets 3′-end extended forms of snRNAs. *Nucleic Acids Res* 2015;**43**:4236–48. https://doi.org/10.1093/nar/gkv240
12. Lubas M, Andersen PR, Schein A *et al.* The human nuclear exosome targeting complex is loaded onto newly synthesized RNA to direct early ribonucleolysis. *Cell Rep* 2015;**10**:178–92. https://doi.org/10.1016/j.celrep.2014.12.026
13. Blackledge NP, Rose NR, Klose RJ. Targeting polycomb systems to regulate gene expression: modifications to a complex story. *Nat Rev Mol Cell Biol* 2015;**16**:643–9. https://doi.org/10.1038/nrm4067
14. Chammas P, Mocavini I, Di Croce L. Engaging chromatin: PRC2 structure meets function. *Br J Cancer* 2020;**122**:315–28. https://doi.org/10.1038/s41416-019-0615-2
15. Xu B, Konze KD, Jin J *et al.* Targeting EZH2 and PRC2 dependence as novel anticancer therapy. *Exp Hematol* 2015;**43**:698–712. https://doi.org/10.1016/j.exphem.2015.05.001
16. Shan Y, Liang Z, Xing Q *et al.* PRC2 specifies ectoderm lineages and maintains pluripotency in primed but not naive ESCs. *Nat Commun* 2017;**8**:672. https://doi.org/10.1038/s41467-017-00668-4
17. van Mierlo G, Veenstra GJC, Vermeulen M *et al.* The complexity of PRC2 subcomplexes. *Trends Cell Biol* 2019;**29**:660–71. https://doi.org/10.1016/j.tcb.2019.05.004
18. Wu H, Zeng H, Dong A *et al.* Structure of the catalytic domain of EZH2 reveals conformational plasticity in cofactor and substrate binding sites and explains oncogenic mutations. *PLoS One* 2013;**8**:e83737. https://doi.org/10.1371/journal.pone.0083737
19. Holoch D, Margueron R. Mechanisms regulating PRC2 recruitment and enzymatic activity. *Trends Biochem Sci* 2017;**42**:531–42. https://doi.org/10.1016/j.tibs.2017.04.003
20. Beringer M, Pisano P, Di Carlo V *et al.* EPOP functionally links elongin and polycomb in pluripotent stem cells. *Mol Cell* 2016;**64**:645–58. https://doi.org/10.1016/j.molcel.2016.10.018
21. Smits AH, Jansen PW, Poser I *et al.* Stoichiometry of chromatin-associated protein complexes revealed by label-free quantitative mass spectrometry-based proteomics. *Nucleic Acids Res* 2013;**41**:e28. https://doi.org/10.1093/nar/gks941
22. Cao R, Zhang Y. SUZ12 is required for both the histone methyltransferase activity and the silencing function of the EED-EZH2 complex. *Mol Cell* 2004;**15**:57–67. https://doi.org/10.1016/j.molcel.2004.06.020
23. Pasini D, Cloos PA, Walfridsson J *et al.* JARID2 regulates binding of the polycomb repressive complex 2 to target genes in ES cells. *Nature* 2010;**464**:306–10. https://doi.org/10.1038/nature08788
24. Vizan P, Beringer M, Ballare C *et al.* Role of PRC2-associated factors in stem cells and disease. *FEBS J* 2015;**282**:1723–35. https://doi.org/10.1111/febs.13083
25. Zhao J, Ohsumi TK, Kung JT *et al.* Genome-wide identification of polycomb-associated RNAs by RIP-seq. *Mol Cell* 2010;**40**:939–53. https://doi.org/10.1016/j.molcel.2010.12.011
26. Kaneko S, Son J, Shen SS *et al.* PRC2 binds active promoters and contacts nascent RNAs in embryonic stem cells. *Nat Struct Mol Biol* 2013;**20**:1258–64. https://doi.org/10.1038/nsmb.2700

27. Beltran M, Yates CM, Skalska L *et al.* The interaction of PRC2 with RNA or chromatin is mutually antagonistic. *Genome Res* 2016;**26**:896–907. https://doi.org/10.1101/gr.197632.115
28. Davidovich C, Cech TR. The recruitment of chromatin modifiers by long noncoding RNAs: lessons from PRC2. *RNA* 2015;**21**:2007–22. https://doi.org/10.1261/rna.053918.115
29. Wang X, Paucek RD, Gooding AR *et al.* Molecular analysis of PRC2 recruitment to DNA in chromatin and its inhibition by RNA. *Nat Struct Mol Biol* 2017;**24**:1028–38. https://doi.org/10.1038/nsmb.3487
30. Kaneko S, Son J, Bonasio R *et al.* Nascent RNA interaction keeps PRC2 activity poised and in check. *Genes Dev* 2014;**28**:1983–8. https://doi.org/10.1101/gad.247940.114
31. Beltran M, Tavares M, Justin N *et al.* G-tract RNA removes polycomb repressive complex 2 from genes. *Nat Struct Mol Biol* 2019;**26**:899–909. https://doi.org/10.1038/s41594-019-0293-z
32. Skalska L, Begley V, Beltran M *et al.* Nascent RNA antagonizes the interaction of a set of regulatory proteins with chromatin. *Mol Cell* 2021;**81**:2944–59. https://doi.org/10.1016/j.molcel.2021.05.026
33. Garland W, Comet I, Wu M *et al.* A functional link between nuclear RNA decay and transcriptional control mediated by the polycomb repressive complex 2. *Cell Rep* 2019;**29**:1800–11. https://doi.org/10.1016/j.celrep.2019.10.011
34. Lewis PW, Muller MM, Koletsky MS *et al.* Inhibition of PRC2 activity by a gain-of-function H3 mutation found in pediatric glioblastoma. *Science* 2013;**340**:857–61. https://doi.org/10.1126/science.1232245
35. Cyrus S, Burkardt D, Weaver DD *et al.* PRC2-complex related dysfunction in overgrowth syndromes: a review of EZH2, EED, and SUZ12 and their syndromic phenotypes. *Am J Med Genet C Semin Med Genet* 2019;**181**:519–31. https://doi.org/10.1002/ajmg.c.31754
36. Kleer CG, Cao Q, Varambally S *et al.* EZH2 is a marker of aggressive breast cancer and promotes neoplastic transformation of breast epithelial cells. *Proc Natl Acad Sci USA* 2003;**100**:11606–11. https://doi.org/10.1073/pnas.1933744100
37. Hoy SM. Tazemetostat: first approval. *Drugs* 2020;**80**:513–21. https://doi.org/10.1007/s40265-020-01288-x
38. Xiao JB, Li XL, Liu L *et al.* The association of semaphorin 5A with lymph node metastasis and adverse prognosis in cervical cancer. *Cancer Cell Int* 2018;**18**:87. https://doi.org/10.1186/s12935-018-0584-1
39. Saxena S, Hayashi Y, Wu L *et al.* Pathological and functional significance of Semaphorin-5A in pancreatic cancer progression and metastasis. *Oncotarget* 2018;**9**:5931–43. https://doi.org/10.18632/oncotarget.23644
40. Ko PH, Lenka G, Chen YA *et al.* Semaphorin 5A suppresses the proliferation and migration of lung adenocarcinoma cells. *Int J Oncol* 2020;**56**:165–77.
41. Wang W, Zhao X, Shao Y *et al.* Mutation-induced DNMT1 cleavage drives neurodegenerative disease. *Sci Adv* 2021;**7**:eabe8511. https://doi.org/10.1126/sciadv.abe8511
42. Hou G, Zhao X, Li L *et al.* SUMOylation of YTHDF2 promotes mRNA degradation and cancer progression by increasing its binding affinity with m6A-modified mRNAs. *Nucleic Acids Res* 2021;**49**:2859–77. https://doi.org/10.1093/nar/gkab065
43. Zhang H, Zhao X, Guo Y *et al.* Hypoxia regulates overall mRNA homeostasis by inducing Met(1)-linked linear ubiquitination of AGO2 in cancer cells. *Nat Commun* 2021;**12**:5416. https://doi.org/10.1038/s41467-021-25739-5
44. Chen C, Zhu C, Huang J *et al.* SUMOylation of TARBP2 regulates miRNA/siRNA efficiency. *Nat Commun* 2015;**6**:8899. https://doi.org/10.1038/ncomms9899
45. Zhu C, Chen C, Huang J *et al.* SUMOylation at K707 of DGCR8 controls direct function of primary microRNA. *Nucleic Acids Res* 2015;**43**:7945–60. https://doi.org/10.1093/nar/gkv741
46. Huang J, Yan J, Zhang J *et al.* SUMO1 modification of PTEN regulates tumorigenesis by controlling its association with the plasma membrane. *Nat Commun* 2012;**3**:911. https://doi.org/10.1038/ncomms1919
47. Pertea M, Kim D, Pertea GM *et al.* Transcript-level expression analysis of RNA-seq experiments with HISAT, StringTie and Ballgown. *Nat Protoc* 2016;**11**:1650–67. https://doi.org/10.1038/nprot.2016.095
48. Trapnell C, Williams BA, Pertea G *et al.* Transcript assembly and quantification by RNA-seq reveals unannotated transcripts and isoform switching during cell differentiation. *Nat Biotechnol* 2010;**28**:511–5. https://doi.org/10.1038/nbt.1621
49. Subramanian A, Tamayo P, Mootha VK *et al.* Gene set enrichment analysis: A knowledge-based approach for interpreting genome-wide expression profiles. *Proc Natl Acad Sci USA* 2005;**102**:15545–50. https://doi.org/10.1073/pnas.0506580102
50. Langmead B, Salzberg SL. Fast gapped-read alignment with Bowtie 2. *Nat Methods* 2012;**9**:357–9. https://doi.org/10.1038/nmeth.1923
51. Zhang Y, Liu T, Meyer CA *et al.* Model-based analysis of ChIP-Seq (MACS). *Genome Biol* 2008;**9**:R137. https://doi.org/10.1186/gb-2008-9-9-r137
52. Shen L, Shao NY, Liu X *et al.* diffReps: detecting differential chromatin modification sites from ChIP-seq data with biological replicates. *PLoS One* 2013;**8**:e65598. https://doi.org/10.1371/journal.pone.0065598
53. Ramirez F, Ryan DP, Gruning B *et al.* deepTools2: a next generation web server for deep-sequencing data analysis. *Nucleic Acids Res* 2016;**44**:W160–5. https://doi.org/10.1093/nar/gkw257
54. Li D, Purushotham D, Harrison JK *et al.* WashU Epigenome Browser update 2022. *Nucleic Acids Res* 2022;**50**:W774–81. https://doi.org/10.1093/nar/gkac238
55. Herzog VA, Reichholf B, Neumann T *et al.* Thiol-linked alkylation of RNA to assess expression dynamics. *Nat Methods* 2017;**14**:1198–204. https://doi.org/10.1038/nmeth.4435
56. Koboldt DC, Zhang Q, Larson DE *et al.* VarScan 2: somatic mutation and copy number alteration discovery in cancer by exome sequencing. *Genome Res* 2012;**22**:568–76. https://doi.org/10.1101/gr.129684.111
57. Bailey TL, Johnson J, Grant CE *et al.* The MEME suite. *Nucleic Acids Res* 2015;**43**:W39–49. https://doi.org/10.1093/nar/gkv416
58. Belmonte-Reche E, Morales JC. G4-iM Grinder: when size and frequency matter. G-Quadruplex, i-motif and higher order structure search and analysis tool. *NAR Genom Bioinform* 2020;**2**:lqz005. https://doi.org/10.1093/nargab/lqz005
59. Kikin O, D'Antonio L, Bagga PS. QGRS Mapper: a web-based server for predicting G-quadruplexes in nucleotide sequences. *Nucleic Acids Res* 2006;**34**:W676–82. https://doi.org/10.1093/nar/gkl253
60. Muhar M, Ebert A, Neumann T *et al.* SLAM-seq defines direct gene-regulatory functions of the BRD4-MYC axis. *Science* 2018;**360**:800–5. https://doi.org/10.1126/science.aao2793
61. Loedige I, Baranovskii A, Mendonsa S *et al.* mRNA stability and m(6)A are major determinants of subcellular mRNA localization in neurons. *Mol Cell* 2023;**83**:2709–25. https://doi.org/10.1016/j.molcel.2023.06.021
62. Ugolini M, Kerlin MA, Kuznetsova K *et al.* Transcription bodies regulate gene expression by sequestering CDK9. *Nat Cell Biol* 2024;**26**:604–12. https://doi.org/10.1038/s41556-024-01389-9
63. Li H, Liefke R, Jiang J *et al.* Polycomb-like proteins link the PRC2 complex to CpG islands. *Nature* 2017;**549**:287–91. https://doi.org/10.1038/nature23881
64. Wang X, Goodrich KJ, Gooding AR *et al.* Targeting of polycomb repressive complex 2 to RNA by short repeats of consecutive guanines. *Mol Cell* 2017;**65**:1056–67. https://doi.org/10.1016/j.molcel.2017.02.003
65. Wang Y, Yu Y, Pang Y *et al.* The distinct roles of zinc finger CCHC-type (ZCCHC) superfamily proteins in the regulation of RNA metabolism. *RNA Biol* 2021;**18**:2107–26. https://doi.org/10.1080/15476286.2021.1909320

66. Benhalevy D, Gupta SK, Danan CH *et al.* The Human CCHC-type zinc finger nucleic acid-binding protein binds G-rich elements in target mRNA coding sequences and promotes translation. *Cell Rep* 2017;**18**:2979–90. https://doi.org/10.1016/j.celrep.2017.02.080
67. Ku M, Koche RP, Rheinbay E *et al.* Genomewide analysis of PRC1 and PRC2 occupancy identifies two classes of bivalent domains. *PLoS Genet* 2008;**4**:e1000242. https://doi.org/10.1371/journal.pgen.1000242
68. Sadanandam A, Rosenbaugh EG, Singh S *et al.* Semaphorin 5A promotes angiogenesis by increasing endothelial cell proliferation, migration, and decreasing apoptosis. *Microvasc Res* 2010;**79**:1–9. https://doi.org/10.1016/j.mvr.2009.10.005
69. Sadanandam A, Varney ML, Kinarsky L *et al.* Identification of functional cell adhesion molecules with a potential role in metastasis by a combination of in vivo phage display and in silico analysis. *OMICS* 2007;**11**:41–57. https://doi.org/10.1089/omi.2006.0004
70. Reisman D, Glaros S, Thompson EA. The SWI/SNF complex and cancer. *Oncogene* 2009;**28**:1653–68. https://doi.org/10.1038/onc.2009.4
71. Maeda D, Mao TL, Fukayama M *et al.* Clinicopathological significance of loss of ARID1A immunoreactivity in ovarian clear cell carcinoma. *Int J Mol Sci* 2010;**11**:5120–8. https://doi.org/10.3390/ijms11125120
72. Luchini C, Veronese N, Solmi M *et al.* Prognostic role and implications of mutation status of tumor suppressor gene ARID1A in cancer: a systematic review and meta-analysis. *Oncotarget* 2015;**6**:39088–97. https://doi.org/10.18632/oncotarget.5142
73. Liu X, Li Z, Wang Z *et al.* Chromatin remodeling induced by ARID1A loss in lung cancer promotes glycolysis and confers JQ1 vulnerability. *Cancer Res* 2022;**82**:791–804. https://doi.org/10.1158/0008-5472.CAN-21-0763
74. Ernst T, Chase AJ, Score J *et al.* Inactivating mutations of the histone methyltransferase gene EZH2 in myeloid disorders. *Nat Genet* 2010;**42**:722–6. https://doi.org/10.1038/ng.621
75. Parreno V, Loubiere V, Schuettengruber B *et al.* Transient loss of polycomb components induces an epigenetic cancer fate. *Nature* 2024; https://doi.org/10.1038/s41586-024-07328-w
76. Flavahan WA, Gaskell E, Bernstein BE. Epigenetic plasticity and the hallmarks of cancer. *Science* 2017;**357**:eaal2380. https://doi.org/10.1126/science.aal2380
77. Chan HL, Morey L. Emerging roles for polycomb-group proteins in stem cells and cancer. *Trends Biochem Sci* 2019;**44**:688–700. https://doi.org/10.1016/j.tibs.2019.04.005

Received: June 24, 2024. **Revised:** January 13, 2025. **Editorial Decision:** January 30, 2025. **Accepted:** February 5, 2025